HIPPOCAMPUS 20:423–446 (2010)

Encoding and Retrieval in a Model of the Hippocampal CA1 Microcircuit

Vassilis Cutsuridis,[1*] Stuart Cobb,[2] and Bruce P. Graham[1*]

ABSTRACT: It has been proposed that the hippocampal theta rhythm (4–7 Hz) can contribute to memory formation by separating encoding (storage) and retrieval of memories into different functional half-cycles (Hasselmo et al. (2002) Neural Comput 14:793–817). We investigate, via computer simulations, the biophysical mechanisms by which storage and recall of spatio-temporal input patterns are achieved by the CA1 microcircuitry. A model of the CA1 microcircuit is presented that uses biophysical representations of the major cell types, including pyramidal (P) cells and four types of inhibitory interneurons: basket (B) cells, axo-axonic (AA) cells, bistratified (BS) cells and oriens lacunosum-moleculare (OLM) cells. Inputs to the network come from the entorhinal cortex (EC), the CA3 Schaffer collaterals and medial septum. The EC input provides the sensory information, whereas all other inputs provide context and timing information. Septal input provides timing information for phasing storage and recall. Storage is accomplished via a local STDP mediated hetero-association of the EC input pattern and the incoming CA3 input pattern on the CA1 pyramidal cell target synapses. The model simulates the timing of firing of different hippocampal cell types relative to the theta rhythm in anesthetized animals and proposes experimentally confirmed functional roles for the different classes of inhibitory interneurons in the storage and recall cycles (Klausberger et al., (2003, 2004) Nature 421:844–848, Nat Neurosci 7:41–47). Measures of recall performance of new and previously stored input patterns in the presence or absence of various inhibitory interneurons are employed to quantitatively test the performance of our model. Finally, the mean recall quality of the CA1 microcircuit is tested as the number of stored patterns is increased. © 2009 Wiley-Liss, Inc.

KEY WORDS: CA1 microcircuit model; storage and recall; pyramidal cell; basket cell; bistratified cell; OLM cell; axo-axonic cell; STDP

INTRODUCTION

Associative memory is one of the oldest artificial neural network (ANN) paradigms. Memory patterns are encoded as the activity patterns across a network of computing units or neurons. Patterns are stored in the memory by Hebbian modification of the connections between the computing units. A memory is recalled when an activity pattern that is a partial or noisy version of a stored pattern is instantiated in the network. Network activity then evolves to the complete stored pattern as appropriate units are recruited to the activity pattern, and noisy units are removed, by threshold-setting of unit activity. Memory capacity for accurate recall is strongly dependent on the form of patterns to be stored, and the Hebbian learning rule employed.

The hippocampus is one of the most widely studied of brain regions, yielding a wealth of data on network architecture, cell types, the anatomy and membrane properties of pyramidal cells and interneurons, and synaptic plasticity (Andersen et al., 2007). Its basic functional role is hypothesized to be the intermediate term storage of declarative memories (Eichenbaum et al., 1999; Wood et al., 1999; Andersen et al., 2007). The hippocampal regions CA3 and CA1 have been proposed to be auto- and heteroassociative memories, respectively (Treves and Rolls, 1994), for the storage of declarative memories.

The hippocampus contains principal excitatory neurons (pyramidal (P) cells in CA3 and CA1 and granule cells (GC) in the dentate gyrus (DG)) and a large variety of inhibitory interneurons (Freund and Buzsaki, 1996; Somogyi and Klausberger, 2005). The microcircuitry these cells form exhibits different rhythmic states in different behavioral conditions. Multiple rhythms, such as theta (4–7 Hz) and gamma (30–100 Hz) oscillations can coexist (Whittington and Traub, 2003). This dynamic complexity presumably corresponds to specific functional processing of information (Axmacher et al., 2006). Much theoretical and computational work has been devoted to trying to understand the cellular and network properties that generate these rhythms (Traub et al., 1999; Buzsaki, 2002). Others have formulated computational models of associative memory based on the architecture and operation of hippocampal areas CA3 and CA1 (Wallenstein and Hasselmo, 1997; Menschik and Finkel, 1998; Kunec et al., 2005). These models include multiple cell types and their connectivity, with cells represented by biophysically-based compartmental models of spiking neurons. These models hypothesize that the theta rhythm modulates episodes of storage of new information and recall of old information in its half cycles (Hasselmo et al., 2002). Kunec et al. (2005) incorporate Hasselmo's (2002) theoretical framework of the separation of storage and recall into separate functional subcycles of theta into a more detailed model of the CA3 microcircuit. Waxing and

An unedited version of this article was originally published online on 1 June 2009. The final, edited version replaced the unedited version on 21 July 2009. Please consider this version to be the version of record.
[1] **Department of Computing Science and Mathematics, University of Stirling, Stirling, United Kingdom;** [2] **Division of Neuroscience and Biomedical Systems, University of Glasgow, Glasgow, United Kingdom**
Grant sponsor: EPSRC project; Grant number: EP/D04281X/1.
*Correspondence to: Dr. Vassilis Cutsuridis, Department of Computing Science and Mathematics, University of Stirling, Stirling, FK9 4LA, United Kingdom. E-mail: vcu@cs.stir.ac.uk or Dr. Bruce P. Graham, Department of Computing Science and Mathematics, University of Stirling, Stirling, FK9 4LA, United Kingdom. E-mail: b.graham@cs.stir.ac.uk
Accepted for publication 17 April 2009
DOI 10.1002/hipo.20661
Published online 1 June 2009 in Wiley InterScience (www.interscience.wiley.com).

waning of GABA-mediated inhibition from the medial septum leads alternately to disinhibition and inhibition of P cells during a theta cycle, corresponding to ideal conditions for pattern recall and pattern storage, respectively. The higher frequency gamma rhythms (30–100 Hz) constitute a basic clock cycle such that patterns of activity for storage and recall correspond to P cells that are active in a particular gamma cycle (Buzsaki and Chrobak, 1995; Lisman and Idiart, 1995; Jensen and Lisman, 1996; Axmacher et al., 2006). Patterns of P cell activity for storage are determined by the spatiotemporal correspondence of direct afferent input from the EC and indirect input via DG onto CA3 P cells and via CA3 P cell input onto CA1 P cells. Such patterns are stored autoassociatively in CA3 by Hebbian modification of recurrent connections between CA3 P cells, and heteroassociatively in CA1 by modification of CA3 input onto CA1 P cells (Hasselmo et al., 2002).

Though these models are much closer to biological neural nets than artificial neural network (ANN) models (Willshaw et al., 1969; Hopfield, 1982; Amit, 1989; Buckingham and Willshaw, 1993; Graham and Willshaw, 1995, 1997; Graham and Willshaw, 1999), they still very much simplify the neuronal circuitry of the mammalian hippocampus. The role of inhibition has largely been confined to basket cells acting to threshold P cell activity during pattern recall (Sommer and Wennekers, 2000, 2001). Other ideas include the possibility that axo-axonic cells provide the negative weights due to pattern storage required in some ANN models of associative memory (Menschik and Finkel, 1998).

The challenge remains to provide functional explanations that include more details of the known microcircuitry. Paulsen and Moser (1998) advanced a conceptual model of how GABAergic interneurons might provide the control structures necessary for phasing storage and recall in the hippocampus. Building on their idea, we propose a functional model of the CA1 microcircuit, including a number of different neuronal types and their specific roles in storage and recall. Our model addresses four important issues: (1) How are storage and recall controlled in the CA1 microcircuit? (2) What roles do the various types of inhibitory interneurons play in the dynamical CA1 information processing? (3) What is the recall performance of new and previously stored patterns in the presence and absence of various types of inhibitory interneurons? (4) What is the mean recall quality of the CA1 microcircuit as the number of stored patterns increases?

Preliminary studies have been previously published in Cutsuridis et al. (2007, 2008a, c) and Graham and Cutsuridis (2009).

MATERIALS AND METHODS

Figure 1 illustrates the simulated microcircuit model of the CA1 network. The model consists of 100 pyramidal (P) cells, 2 basket (B) cells, 1 bistratified (BS) cell, 1 axo-axonic (AA) cell, and 1 oriens lacunosum moleculare (OLM) cell. All simulations were performed using NEURON (Hines and Carnevale, 1997) running on a PC under Windows XP and on a cluster of 64 nodes with MPI (message passing protocol).

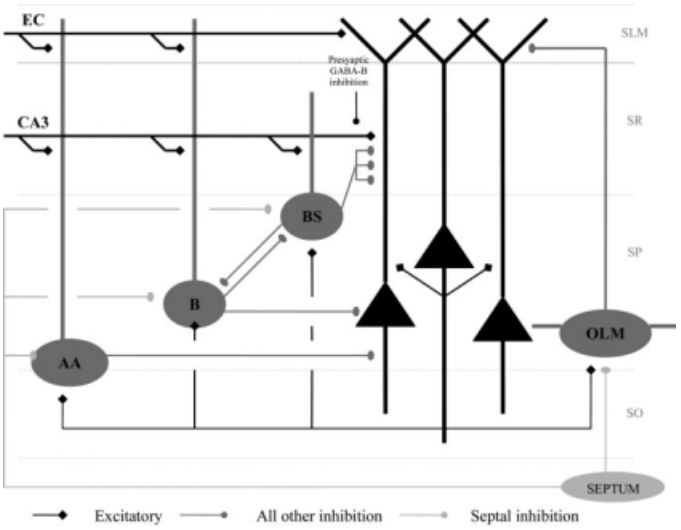

FIGURE 1. Hippocampal CA1 microcircuit showing major cell types and their connectivity. Black filled triangles: pyramidal cells. Dark gray filled circles: CA1 inhibitory interneurons. EC: entorhinal cortex input; CA3: CA3 Schaffer collateral input; AA: axo-axonic cell; B: basket cell; BS: bistratified cell; OLM: oriens lacunosum-moleculare cell; SLM: stratum lacunosum moleculare; SR: stratum radiatum; SP: stratum pyramidale; SO: stratum oriens. Light gray filled circles: Septal GABA inhibition.

Simplified morphologies including the soma, apical and basal dendrites and a portion of axon, were used for each cell type. The biophysical properties of each cell were adapted from cell types reported in the literature (Poirazzi et al., 2003a, 2003b; Saraga et al., 2003; Santhakumar et al., 2005). The complete mathematical formalism of the model is described in the appendix. Schematic representations of the model cells, and their responses to current injections are depicted in Figure 2. The dimensions of the somatic, axonic, and dendritic compartments of the model cells are presented in Table 1. The parameters of all passive and active ionic conductances used in the model are listed in Tables 2–4. The synaptic waveform parameters are given in Table 5 and synaptic conductances are listed in Table 6.

Pyramidal Cells

Each P cell had 15 compartments, each containing a calcium pump and buffering mechanism, calcium activated slow AHP and medium AHP potassium (K^+) currents, an HVA L-type Ca^{2+} current, an HVA R-type Ca^{2+} current, an LVA T-type Ca^{2+} current, an h current, a fast sodium and a delayed rectifier K^+ current, a slowly inactivating K^+ M current and a fast inactivating K^+ A current (Poirazzi et al., 2003a, 2003b).

Each P cell's soma rested in the stratum pyramidale (SP), while its dendrites extended across the strata from stratum oriens (SO) to striatum radiatum (SR) and stratum lacunosum-moleculare (SLM). Each pyramidal cell received somatic synap-

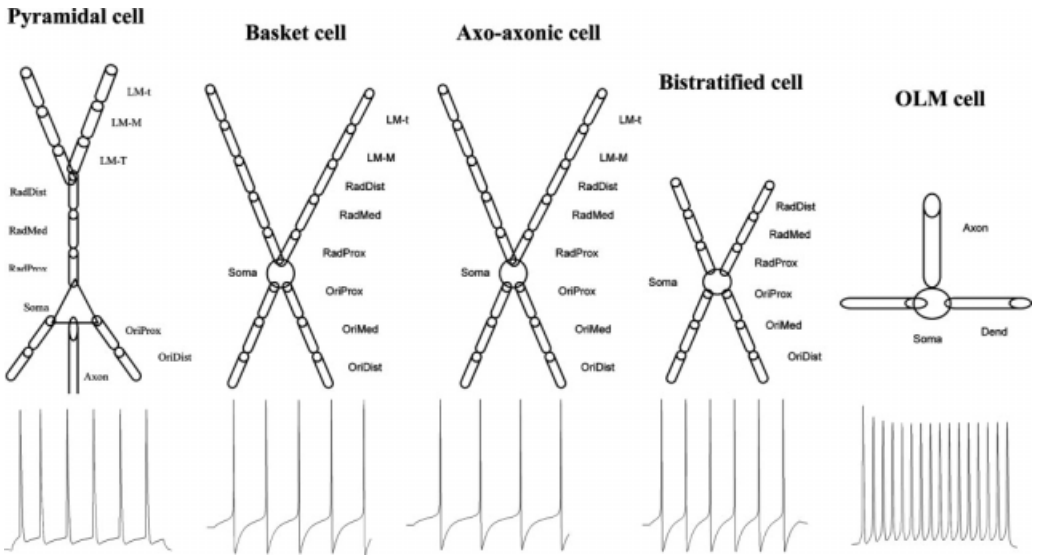

FIGURE 2. Compartmental structure models for the different cell types, plus their firing properties in response to depolarizing current injection (not shown; amplitude: 0.1 nA; duration: 200 ms). From left-to-right: pyramidal cell (PC), axo-axonic cell (AAC), basket cell (BC), bistratified cell (BSC), oriens lacunosum moleculare cell (OLM). LM-t: lacunosum moleculare thin compartment; LM-M: lacunosum moleculare medium compartment; LM-T: lacunosum moleculare thick compartment; OriProx: oriens-proximal compartment; OriMed: oriens medial compartment; OriDist: oriens distal compartment; RadProx: radiatum proximal compartment; RadMed: radiatum medial compartment; RadDist: radiatum distal compartment; Dend: basal OLM cell compartment.

tic inhibition from the basket cells, mid-dendritic excitation from CA3, distal apical excitation from the entorhinal cortex (EC), proximal excitation from around 1% of other pyramidal cells in the network (recurrent collaterals) (Amaral and Lavenex, 2007, Andersen et al., 2007), axonic inhibition from the axoaxonic cell, spatially-distributed (six contacts) mid-dendritic

TABLE 1.

Structure of Model Cells

Dimensions	Pyramidal cell	Axo-axonic cell	Basket cell	Bistratified cell	OLM cell
Soma					
Diameter, μm	10	10	10	10	10
Length, μm	10	20	20	20	20
Total number of compartments (soma + dendritic compartments)	15	17	17	13	4
Dendritic compartments and dimensions (diameter × length, μm^2)					
Basal dendrite					3 × 250
Axon	1 × 150				1.5 × 150
Thick proximal SR dendrite	4 × 100				
Thick medium SR dendrite	3 × 100				
Thick distal SR dendrite	2 × 200				
Proximal SO dendrite	2 × 100				
Distal SO dendrite	1.5 × 200				
Thick SLM dendrite	2 × 100				
Medium SLM dendrite	1.5 × 100				
Thin SLM dendrite	1 × 50				
Thick SR dendrite		4 × 100	4 × 100	4 × 100	
Medium SR dendrite		3 × 100	3 × 100	3 × 100	
Thin SR dendrite		2 × 200	2 × 200	2 × 200	
Medium SLM dendrite		1.5 × 100	1.5 × 100		
Thin SLM dendrite		1 × 100	1 × 100		
Thick SO dendrite		2 × 100	2 × 100	2 × 100	
Medium SO dendrite		1.5 × 100	1.5 × 100	1.5 × 100	
Thin SO dendrite		1 × 100	1 × 100	1 × 100	

TABLE 2.

Passive Parameters and Active Ionic Conductances of Channels for all Compartments of Pyramidal Model Cells

Mechanism	Soma	Axon	OriProx	OriDist	RadProx	RadMed	RadDist	LM
C_m, $\mu F/cm^2$	1	1	1	1	1	1	1	1
R_m, Ohm cm^2	20,000	20,000	20,000	20,000	20,000	20,000	20,000	20,000
R_a, Ωcm	150	150	150	150	150	150	150	150
Leak conductance [S/cm^2]	0.0002	0.000005	0.000005	0.000005	0.000005	0.000005	0.000005	0.000005
Sodium conductance [S/cm^2]	0.007	0.1	0.007	0.007	0.007	0.007	0.007	0.007
Delayed rectifier K^+ conductance [S/cm^2]	0.0014	0.02	0.000868	0.000868	0.000868	0.000868	0.000868	0.000868
Proximal A-type K^+ conductance [S/cm^2]	0.0075	–	0.0075	0.0075	0.015	0	0	–
Distal A-type K^+ conductance [S/cm^2]	–	–	0	0	0	0.03	0.045	0.049
M-type K^+ conductance [S/cm^2]	0.06	0.03	0.06	0.06	0.06	0.06	0.06	–
I_h conductance [S/cm^2]	0.00005	–	0.00005	0.0001	0.0001		0.0002	0.00035
$V_{half,h}$ (mV)	−73	–	−81	−81	−82	−81	−81	–
L-type Ca^{2+} conductance [S/cm^2]	0.0007	–	0.000031635	0.000031635	0.000031635	0.0031635	0.0031635	–
T-type Ca^{2+} conductance [S/cm^2]	0.00005	–	0.0001	0.0001	0.0001	0.0001	0.0001	–
R-type Ca^{2+} conductance [S/cm^2]	0.0003	–	0.00003	0.00003	0.00003	0.00003	0.00003	–
Ca^{2+}-dependent sAHP K^+ conductance [S/cm^2]	0.0005	–	0.0005	0.0005	0.0005	0.0005	0.0005	–
Ca^{2+}-dependent mAHP K^+ conductance [S/cm^2]	0.09075	–	0.033	0.033	0.033	0.033	0.0041	–
E_L (mV)	−70	−70	−70	−70	−70	−70	−70	−70
E_{Na} (mV)	50	50	50	50	50	50	50	50
E_h, (mV)	−10	–	−10	−10	−10	−10	−10	−10
E_{Ca}, (mV)	140	–	140	140	140	140	140	–
E_K (mV)	−80	−80	−80	−80	−80	−80	−80	−80

synaptic inhibition from the bistratified cells population (Buhl et al., 1994a), and distal synaptic inhibition on each SLM dendritic branch from the OLM cell.

Axo-Axonic Cells

Each AA cell had 17 compartments, which included a leak conductance, a sodium current, a fast delayed rectifier K^+ current, an A-type K^+ current, L- and N-type Ca^{2+} currents, a Ca^{2+}-dependent K^+ current and a Ca^{2+}- and voltage-dependent K^+ current (Santhakumar et al., 2005).

As with the P cells in the network, each AA's cell body rested primarily in the SP, while its dendrites extended across the strata from SO to SR and SLM. Axo-axonic cells received excitatory inputs from the EC perforant path to their SLM dendrites and excitatory inputs from the CA3 Schaffer collateral to their SR dendrites. In addition, the axo-axonic cells received inputs from active CA1 pyramidal cells in their SR medium and thick dendritic compartments as well as inhibitory input from the septum in their SO thick dendritic compartments (Ganter et al., 2004; Andersen et al., 2007).

Basket Cells

Each B cell had 17 compartments, containing a leak conductance, a sodium current, a fast delayed rectifier K^+ current, an A-type K^+ current, L- and N-type Ca^{2+} currents, a Ca^{2+}-

TABLE 3.

Passive Parameters and Active Ionic Conductances of Channels for all Compartments Of Axo-Axonic, Basket, and Bistratified Model Cells

Mechanism	Axo-axonic cell	Basket cell	Bistratified cell
C_m, $\mu F/cm^2$	1.4	1.4	1.4
R_a, Ωcm	100	100	100
Leak conductance [S/cm^2]	0.00018	0.00018	0.00018
Sodium [S/cm^2]	0.15	0.2	0.3
Delayed rectifier K^+ [S/cm^2]	0.013	0.013	0.013
A-type K^+ [S/cm^2]	0.00015	0.00015	0.00015
L-type Ca^{2+} [S/cm^2]	0.005	0.005	0.005
N-type Ca^{2+} [S/cm^2]	0.0008	0.0008	0.0008
Ca^{2+}-dependent K^+ [S/cm^2]	0.000002	0.000002	0.000002
Ca^{2+}- and voltage-dependent K^+ [S/cm^2]	0.0002	0.0002	0.0002
Time constant for decay of intracellular Ca^{2+} [ms]	10	10	10
Steady-state intracellular Ca^{2+} concentration (mM)	5.e-6	5.e-6	5.e-6
E_{Na}, (mV)	55	55	55
E_K, (mV)	−90	−90	−90
E_{Ca}, (mV)	130	130	130
E_L, (mV)	−60	−60	−60
$[Ca^{2+}]_0$ (mM)	2	2	2

TABLE 4.

Passive Parameters and Active Ionic Conductances of Channels for all Compartments Of Olm Model Cells

	Compartment		
Mechanism	Soma	Dendrite	Axon
C_m, $\mu F/cm^2$	1.3	1.3	1.3
R_a, Ωcm	150	150	150
Leak conductance. S/cm^2	0.00005	0.00005	0.00005
E_L, mV	−70	−70	−70
Sodium, S/cm^2	0.0107	0.0234	0.01712
E_{Na}, mV	90	90	90
Delayed rectifier K^+, S/cm^2	0.0319	0.046	0.05104
E_K, mV	−100	−100	−100
A-type K^+, S/cm^2	0.0165	0.004	–
E_A, mV	−100	−100	−100
I_h, S/cm^2	0.0005	–	–
E_h, mV	−32.9	−32.9	−32.9

dependent K^+ current, and a Ca^{2+}- and voltage-dependent K^+ current (Santhakumar et al., 2005). As before, all B cells' somas rested in SP, whereas their dendrites extended from SO to SLM. All B cells received excitatory connections from the EC to their distal SLM dendrites, from the CA3 Schaffer collaterals to their medium SR dendrites and from active pyramidal cells to their medium and thick SR dendritic compartments and inhibitory connections from neighboring B and BS cells in their soma (Freund and Buzsaki, 1996) and from the medial septum in their SO thick dendritic compartments.

Bistratified Cells

Each BS cell had 13 compartments, which included the same ionic currents as the B and AA cells. All BS cells' somas rested in the SR, whereas their dendrites extended from SO to SR. All BS cells received excitatory connections from the CA3 Schaffer collaterals in their medium SR dendritic compartments and from the active pyramidal cells in their thick SO dendritic compartments and inhibitory connections from the medial septum in their thick SO dendritic compartments and from neighboring B and BS cells in their somas.

TABLE 5.

Synaptic Parameters

Mechanisms	AMPA	NMDA	GABA-A	GABA-B
Rise [ms]	0.5	2.3	1	35
Fall [ms]	3	100	8	100
Reversal potential [mV]	0	0	−75	−75

Olm Cells

Each OLM cell had four compartments, which included a sodium (Na^+) current, a delayed rectifier K^+ current, an A-type K^+ current, and an h-current (Saraga et al., 2003). Each OLM cell's soma and basal dendrites rested in SP, whereas its axon extended from SP to SLM. Each OLM cell received excitatory connections from the active pyramidal cells in their basal dendrites as well as inhibitory connections from the medial septum in their soma.

Presynaptic GABA-B Inhibition

Experimental data have shown that activation of presynaptic GABA-B receptors inhibits glutamatergic transmission in stratum radiatum pyramidal cell synapses in the hippocampus (Ault and Nadler, 1982; Colbert and Levy, 1992). However, application of GABA-B agonists to pyramidal cell synapses in SLM does not disrupt transmission at these perforant path synapses (Ault and Nadler, 1982; Colbert and Levy, 1992). Molyneaux and Hasselmo (2002) have recently shown that the pre-

TABLE 6.

Synaptic Conductance Parameters (in MicroSiemens). Text in Parenthesis Signifies the Type of Postsynaptic Receptor

		Postsynaptic				
	EC CA3 Septum	Pyr	AAC	BC	BSC	OLM
Presynaptic	EC	0.001 (AMPA)	0.00015 (AMPA)	0.00015 (AMPA)	0.00015 (AMPA)	
	CA3	0.0015 or 0.0005 (AMPA) 0.0005 (NMDA)	0.00015 (AMPA)	0.00015 (AMPA)	0.00015 (AMPA)	
	Septum		0.02 (GABA-A)	0.02 (GABA-A)	0.0002 (GABA-A)	0.0002 (GABA-A)
	Pyr	0.001 (AMPA)	0.0005 (AMPA	0.0005 (AMPA)	0.0005 (AMPA)	0.0005 (AMPA)
	AAC	0.04 (GABA-A)				
	BC	0.02 (GABA-A)		0.001 (GABA-A)	0.02 (GABA-A)	
	BSC	0.002 (GABA-A) 0.0004 (GABA-B)		0.01 (GABA-A)		
	OLM	0.04 (GABA-A) 0.0004 (GABA-B)				

synaptic inhibition from activation of GABA-B receptors is sufficiently rapid to change within a theta cycle. Cyclical changes during theta in the strength of synaptic input from the EC perforant path versus the CA3 Schaffer collateral synaptic input have also been reported (Brankack et al., 1993; Wyble et al., 2000).

In the model, we propose that these cyclical theta changes are due to the presynaptic GABA-B inhibition to CA3 Schaffer collateral input to CA1 P cells' synapses, which is active during the storage cycle and inactive during recall. This is modeled simply as a reductive scaling during storage of the potentiated P cell SR synaptic conductance achieved by the local STDP learning rule [Eq. (4) in SYNAPTIC PLASTICITY section].

Model Inputs

Inputs to the CA1 model came from the medial septum (MS), entorhinal cortex (EC) and CA3 Schaffer collaterals. The EC input was modeled as the firing of 20 entorhinal cortical cells at an average gamma frequency of 40 Hz (spike trains only modeled and not the explicit cells), and the CA3 input was modeled with the same gamma frequency spiking of 20 out of 100 CA3 pyramidal cells (Appendix for details). P, B, AA, BS cells received CA3 input in their medial SR dendrites, whereas P, B and AA cells received also the EC layer III input in their apical LM dendrites. EC inputs preceded CA3 inputs by 9 ms on average, in accord with experimental data showing that the conduction latency of the EC-layer III input to CA1 LM dendrites is less than 9 ms (ranging between 5 and 8 ms), whereas the conduction latency of EC-layer II input to CA1 radiatum dendrites via the di/tri-synaptic path is greater than 9 ms (ranging between 12 and 18 ms) (Leung et al., 1995; Soleng et al., 2003).

MS input, which was modeled with the rhythmic firing of 10 septal cells (Appendix for details) provided GABA-A inhibition to all INs in the model (strongest to B and AA). MS input was phasic at theta rhythm and was on for 125 ms during the retrieval phase.

Synaptic Properties

In the model, AMPA, NMDA, GABA-A, and GABA-B synapses were considered. GABA-A were present in all strata, whereas GABA-B were present in medium and distal SR and SLM dendrites. AMPA synapses were present in strata LM (EC connections) and radiatum (CA3 connections), whereas NMDA were present only in stratum radiatum (CA3 connections).

Synaptic Plasticity

Although synaptic plasticity is linked with NMDA receptors and Ca^{2+} dynamics, we do not attempt to model the detailed molecular mechanisms underlying synaptic plasticity, but instead we concentrate on the precise activity patterns required to induce synaptic plasticity. During storage an STDP learning rule was applied at CA3-AMPA synapses on P cells' medial SR dendrites, where presynaptic CA3 input spike times were compared with the postsynaptic voltage response to determine an instantaneous change in the synaptic conductance, g:

$$g = g + w.(1 + A) \tag{1}$$

$$A = (w_{\max} - w - A) \times p \times e^{\Delta t/\tau_p} \quad \text{if} \quad \Delta t = t_{\text{post}} - t_{\text{pre}} \geq 0 \tag{2}$$

$$A = A \times (1 - d \times e^{\Delta t/\tau_d}) \quad \text{if} \quad \Delta t = t_{\text{post}} - t_{\text{pre}} < 0 \tag{3}$$

where τ_p = 17 ms and τ_d = 34 ms are the potentiation and depression effectiveness time constants, respectively. According to this rule, effective synaptic strength is the product of the weight, w, and the factor $1+A$, where A is always greater or equal to 0 and represents the degree of potentiation [Eq. (1)]. Potentiation [Eq. (2)] is additive (pre before post adds a positive number to A) and saturates at an effective weight, $w_{\max}$. Depression [Eq. (3)] is multiplicative (post before pre multiplies A by a factor in the range 0 to 1) and can return the synaptic strength to the original weight, w.

During storage the CA3-AMPA synaptic conductance suppression by the putative GABA-B inhibition present during this phase was implemented simply by scaling so that effective conductance g' was:

$$g' = g_s \times g \tag{4}$$

where g_s is the scaling factor (set to 0.4 in the presented simulations). During recall, g' was simply equal to g.

Network Training and Testing

To provide a ground state from which to test storage and recall, firstly a set of patterns are stored without recourse to the STDP learning rule by generating a weight matrix based on a clipped Hebbian learning rule, and using the weight matrix to prespecify the CA3 to CA1 PC connection weights. Without loss of generality, the input (CA3) and output (CA1) patterns were assumed to be the same, with each pattern consisting of 20 randomly chosen PCs out of the population of 100. The 100 by 100 dimensional weight matrix was created by setting matrix entry (i, j), w_{ij} = 1 if input PC i and output PC j are both active in the same pattern pair; otherwise weights are 0. Any number of pattern pairs could be stored to create this binary weight matrix. The matrix was applied to our network model by connecting a CA3 input to a CA1 PC with a high AMPA conductance (g_{AMPA} = 1.5 nS) if their connection weight was 1, or with a low conductance (g_{AMPA} = 0.5 nS) if their connection was 0. This approach is in line with experimental evidence that such synapses are 2-state in nature (Petersen et al., 1998).

During storage, the synaptic conductances of each P cell's SR CA3-AMPA synapses were allowed to change according to the learning rule explained above. Weights were initialized according to the predefined weight matrix and were allowed to change according to the clipped STDP rule. The low conductance state (g_{AMPA} = 0.5 nS) was the minimum weight that

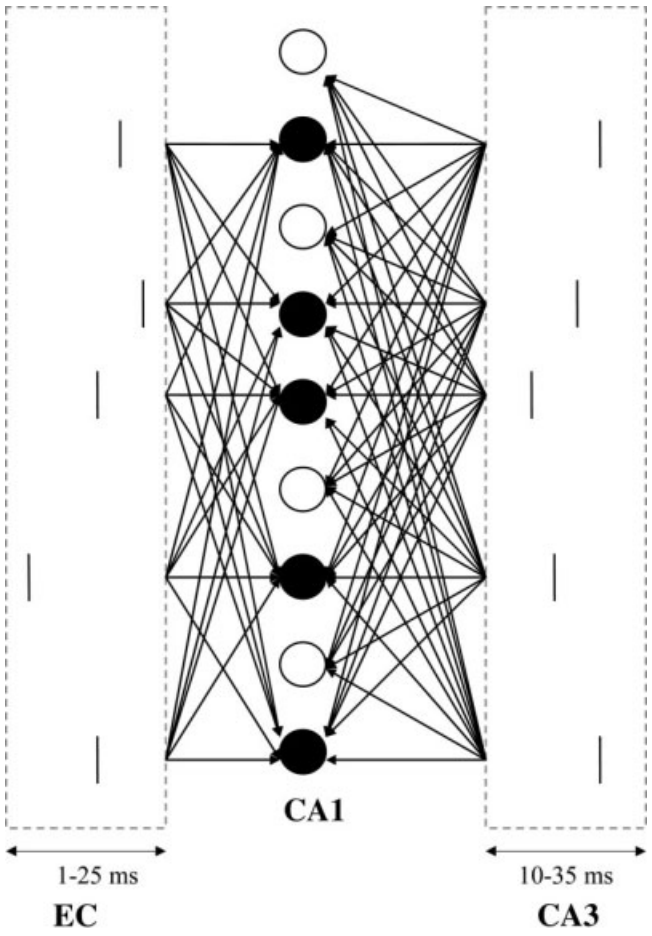

FIGURE 3. Model inputs to CA1 microcircuit. EC: entorhinal cortex input. The input arrives asynchronously in CA1 LM P cell dendrites (not shown) between 1 and 25 ms. A randomly selected subset of P cells receive the EC input. The CA3 input arrives asynchronously in CA1 SR P cell dendrites between 10 and 35 ms (that is, beginning 9 ms after the EC input). All P cells nonselectively receive the CA3 input.

could be achieved by LTD, whereas the high conductance state (g_{AMPA} = 1.5 nS) was the saturated value that could be achieved by long-term potentiation (LTP).

During each recall cycle the STDP learning rule was switched off. The conductance values from the last gamma cycle of the storage subcycle were used during the recall phase. This allows for the rapid testing of the learnt weights without trying to model the long time course of the molecular expression of LTP/LTD.

Recall Performance Metric

The recall performance metric used for measuring the distance between the recalled output pattern, B, from the required output pattern, B^*, was the correlation (i.e., degree of overlap) metric, calculated as the normalized dot product:

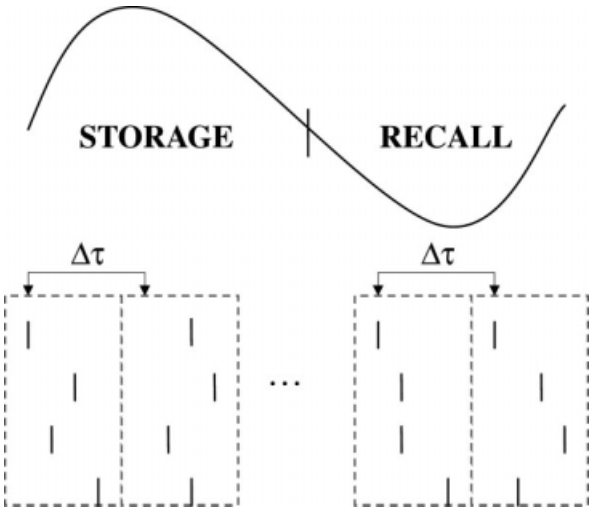

FIGURE 4. Graphical representation of input presentation in the model. Inputs are presented continuously at gamma frequency, throughout the storage and recall cycles of the theta rhythm. Each input window (gray rectangular window) is repeated every Δτ = 25 ms.

$$C = \frac{B \times B^*}{\left(\sum_{i=1}^{N_B} B_i \times \sum_{j=1}^{N_B} B_j^*\right)^{1/2}} \quad (5)$$

where N_B is the number of output units. The correlation takes a value between 0 (no correlation) and 1 (the vectors are identical). The higher the correlation, the better the recall performance.

RESULTS

Storage and Recall Mechanisms

It has been hypothesized that the hippocampal theta rhythm (4–7 Hz) can contribute to memory formation by separating encoding and retrieval of memories into different functional half-cycles (Hasselmo et al., 2002). Previous studies have shown that the septum contains GABAergic and cholinergic neurons that oscillate in a theta rhythm, and have been implicated in pacing the theta rhythm within the hippocampus (Stewart and Fox, 1990). However, the timescales where cholinergic cells operate are too slow to affect the dynamics during the theta period (Hasselmo and Fehlau, 2001). For this reason, only the GABAergic effects of the septum are considered in our study. We will now discuss how the model stores and recalls an input pattern during a theta cycle. Figure 5 summarizes each functional cycle and how the components of the network interact.

Storage cycle

During the storage cycle of the theta (Fig. 5A), we propose the following: an EC input pattern arrives at the apical SLM

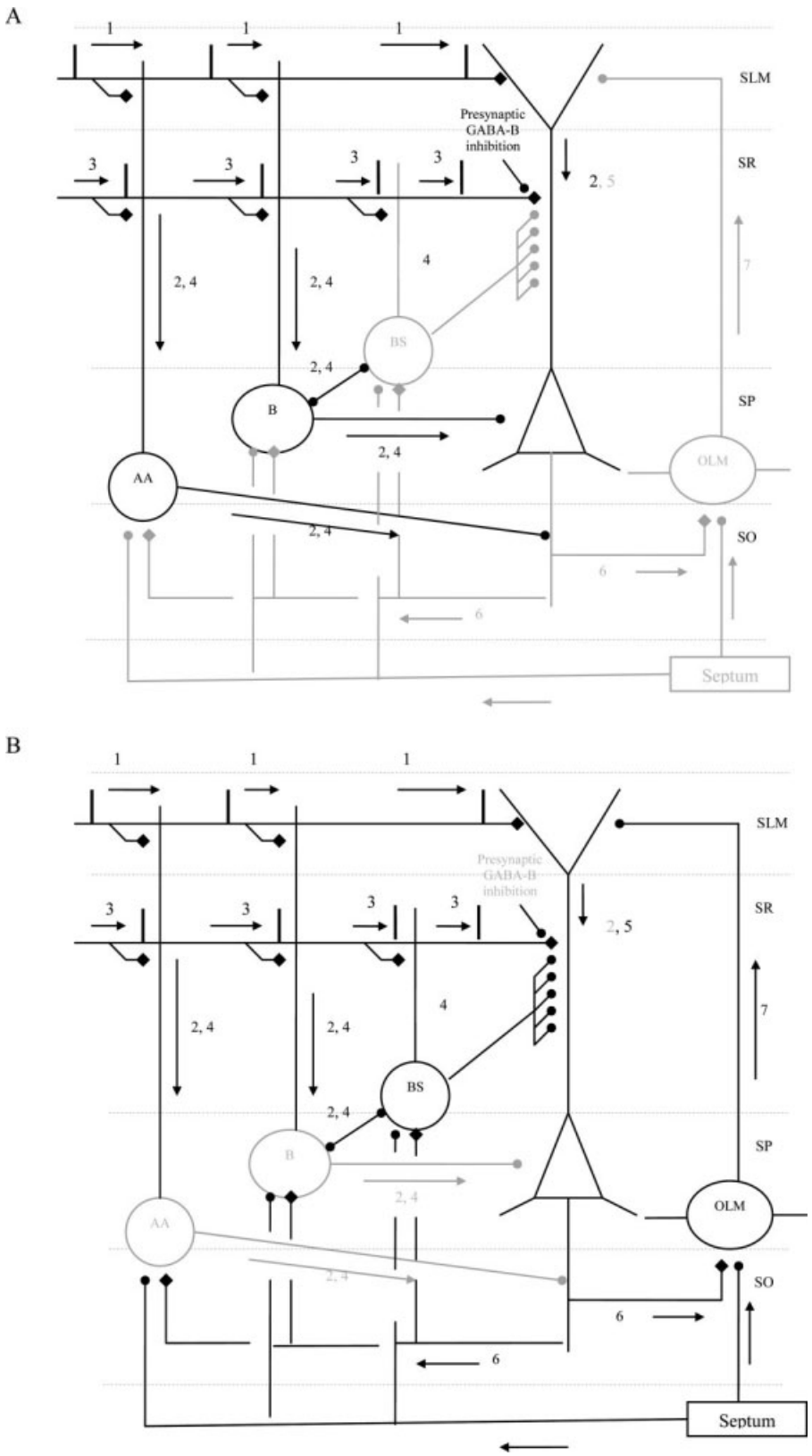

FIGURE 5. Active network pathways during (A) storage cycle and (B) recall cycle. Only black solid lined cells and pathways are active in each cycle. Numbers above and next to pathways indicate the temporal order of information processing during each cycle.

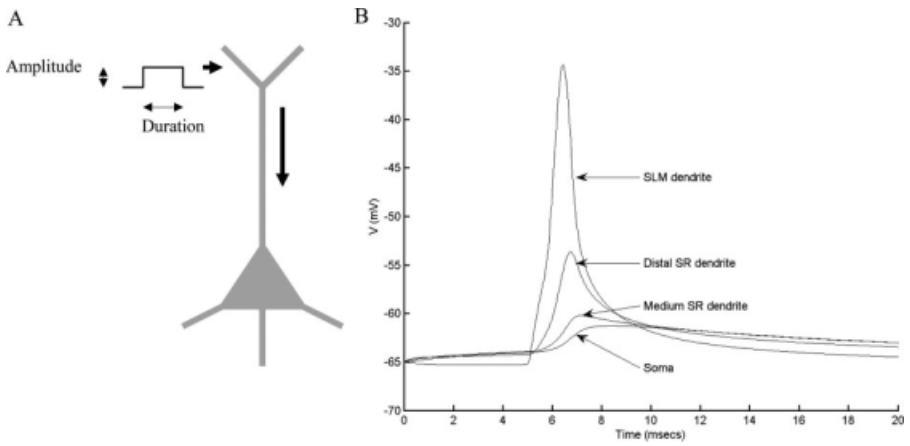

FIGURE 6. Attenuation of SLM generated EPSPs. (A) Representation of reduced CA1 pyramidal cell including applied depolarizing current injection pulse. Pulse amplitude: 0.4 nA; pulse duration: 1 ms. The site of injection was the stratum lacunosum moleculare (SLM) dendrites. (B) Simulated EPSPs recorded at four separate locations: an SLM dendrite (450 μm from the soma), a distal stratum radiatum (SR) dendrite (300 μm from the soma), a medial SR dendrite (150 μm from the soma) and the soma.

dendrites of the B, AA and P cells at time t_i, whereas an indirect CA3 input pattern via the di/trisynaptic loop arrives at the medium SR dendrites of the B, AA, BS and P cells at time $t_i + \Delta t$ (mean $\Delta t = 9$ ms (Leung et al., 1995)). In the B and AA cells, the EC input is strong enough to induce an action potential in their soma. Furthermore, the GABAergic cell population of the medial septum is minimally active and therefore transmits the least amount of inhibition to the CA1 inhibitory interneurons. These active CA1 inhibitory cells are free to do several things. First, the axo-axonic and basket cells exert tight inhibitory control on the axons and somas of the pyramidal cells, thus, preventing them from firing during the storage cycle (Klausberger et al., 2003). Second, the basket cells exert powerful inhibitory control to neighboring basket cells and bistratified cells, which prevents the latter from firing during the storage cycle. The bistratified cells are thus 180° out-of-phase with the basket and axo-axonic cells (Klausberger et al., 2004).

Since place cells in CA1 were found to be maintained solely by direct input from EC and CA1 (Brun et al., 2002), we infer that the CA3 input to P cells provides the contextual information (e.g., familiarity of environment), whereas the EC input to P cells provides the sensory information (e.g., current location). Since there is no topography in CA1 (Amaral and Lavenex, 2007), during the storage cycle, 20% of the P cells in the network are randomly selected to receive the EC input pattern in their apical SLM dendrites. The summed postsynaptic potentials (PSP) generated in the SLM dendrites are attenuated on their way to the soma and axon (Fig. 6), but if coinciding with CA3 input, provide a sufficient depolarized potential in the SR dendrites to drive STDP (Fig. 7); (Stuart and Spruston, 1998; Magee and Cook, 2000; Golding et al., 2005). The B and AA cell mediated inhibition prevents the PSP from causing P cell firing. This inhibition also hyperpolarizes the P cell soma, axon and proximal dendrites of those P cells that do not receive the EC input, preventing them from participating in STDP.

In contrast to the EC input, all P cells in the network are activated by the CA3 input in their medial SR dendrites. The relative timing between the incoming CA3 Schaffer collateral spike and the EC PSP in the SR dendrites will induce LTP or LTD via a local STDP rule (section SYNAPTIC PLASTICITY). The amplitude of the CA3 input is reduced (putatively by presynaptic GABA-B inhibition), hence, P cells not receiving EC input should not exhibit CA3 synaptic plasticity as no depolarizing postsynaptic signal is generated (Fig. 7).

Recall cycle

The recall cycle (Fig. 5B) begins as the presynaptic GABA-B inhibition to CA3 Schaffer collateral input to P cell synapses declines and GABAergic cells of the septum approach maximum activity. Because of this septal input, the basket and axo-axonic cells are now inhibited, releasing pyramidal cells, bistratified cells and OLM cells from inhibition. Pyramidal cells may now fire more easily, thus, allowing previously learned patterns to be recalled.

During the recall cycle, the CA3 Schaffer collateral input plays the role of a cueing mechanism. If the CA3 input excited a pyramidal cell during this time, any synapses that were strengthened during the storage cycle will be activated, recalling the memory. Because the CA3 input is directed to all P cells, which potentially activates unwanted P cells and hence spurious memories are recalled, the role of the bistratified cells is to ensure that these spurious cells will be silenced by broadcasting a nonspecific inhibitory signal to all P cells in the network.

In our model, as it has been previously suggested by Hasselmo and coworkers (2002), during recall the entorhinal cortical input provides a weak background excitation to the CA1 region that aids the recall process, causing depolarized cells to fire. However, this excitation can potentially give rise to unwanted or similar memories. In our model, P cells, after

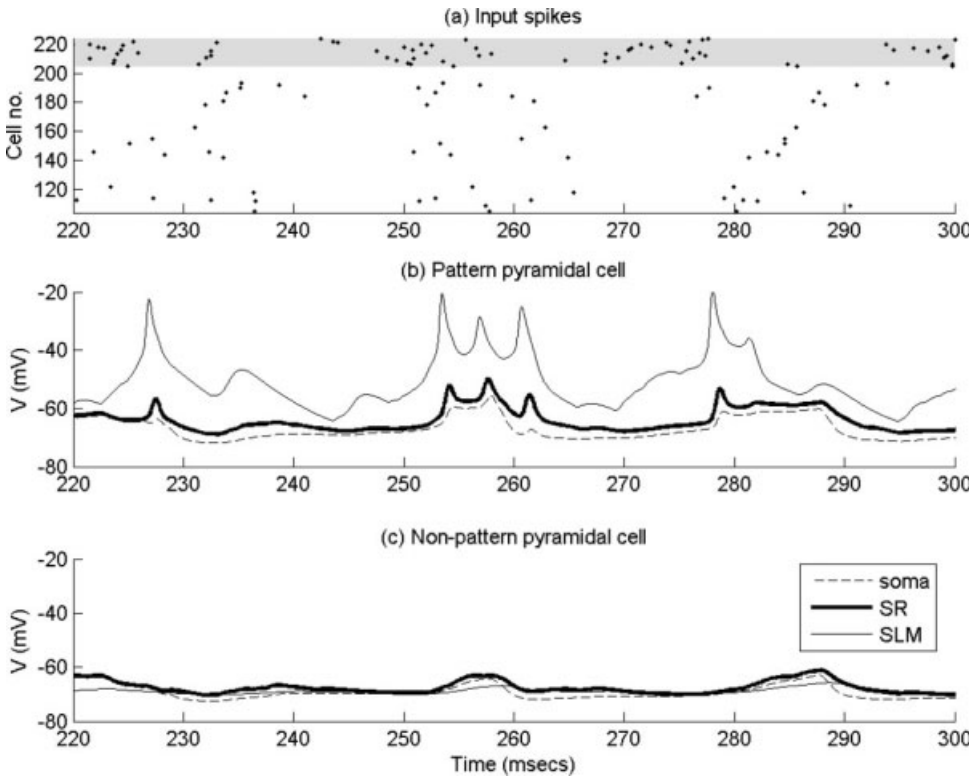

FIGURE 7. Post-synaptic signals in CA1 pyramidal cells in response to EC and CA3 inputs. (a) The inputs are presented three times as groups of spiking randomly distributed over a 25 ms window, with an EC group starting 9 ms before a CA3 group. CA3 input is presented only once (10–35 ms). In the raster plot, the top 20 cells are the EC input (light grey background), and the remaining 100 cells are the CA3 input. (b) The voltage response in the SLM, SR and soma regions of a CA1 pyramidal cell that is receiving both the EC and CA3 inputs is shown. The EC input causes large voltage transients in the SLM, which propagate, in attenuated form, to the SR dendrites. At times 227 ms, 254 ms, 258 ms, 262 ms, and 279 ms the voltage in the SR dendrite passes the STDP threshold of −55 mV. CA3 inputs occurring a short time before these peaks will undergo LTP, whereas those occurring just after the peaks will undergo LTD. (c) The voltage reponses in a P that is only receiving CA3 input. The voltage in the SR dendrite stays well below the STDP threshold and so no synapses are changed.

being released by the basket and axo-axonic cell inhibition, excite the OLM cells. This excitation was assumed strong enough to overcome the OLM septal inhibition. In return, the OLM cells strongly inhibit the distal SLM dendrites of the P cells (Freund and Buzsaki, 1996), where the direct entorhinal input arrives, thus, preventing unwanted or similar memories from being recalled (Kunec et al., 2005).

Model Cell Phase Relationships

As mentioned above, storage and recall phases represent two functionally separated subcycles of the hippocampal theta rhythm (Hasselmo et al., 2002). Recent experimental data showed that during a given behavioral brain state, interneurons of a given type exhibit similar firing patterns, whereas during two distinct brain states, interneurons of the same class show different firing patterns. These results suggested potential roles for specific interneuron types in timing and synchronization of pyramidal cell discharge (Cobb et al., 1995) by structuring the activity of pyramidal cells via their receptive target domains (Somogyi and Klausberger, 2005). Furthermore, it has been shown that the activity of different neuronal types in CA1 is modulated at specific phases relative to the theta rhythm (Klausberger et al., 2003, 2004; Somogyi and Klausberger, 2005). Given that P cell firing is biased towards the recall phase (e.g., place cells firing when a rat is in a familiar location), then it follows that B cells and AA cells fire in phase with the encoding (storage) cycle of the theta rhythm, whereas the P cells, BS cells, OLMs and GABAergic MS input to CA1 fire on the recall cycle (180° out of phase).

Figure 8 shows the phase relationships of four types of CA1 interneurons and CA1 pyramidal cells with respect to the theta oscillation (0–250 ms corresponding to 0–360° of theta cycle). Model basket and axo-axonic cells fire only during the storage phase of theta, whereas the OLM, bistratified and pyramidal cells fire only during the recall phase of theta. The simulated cell phase relationships are in accordance with recent experimental data (Klausberger et al., 2003, 2004; Somogyi and Klausberger, 2005). The functional roles of these cell types in storage and recall have been detailed in the previous section.

Recall of Previously Stored Patterns

Firstly, we will consider the role of interneurons in the recall of previously stored patterns. As detailed in Materials and

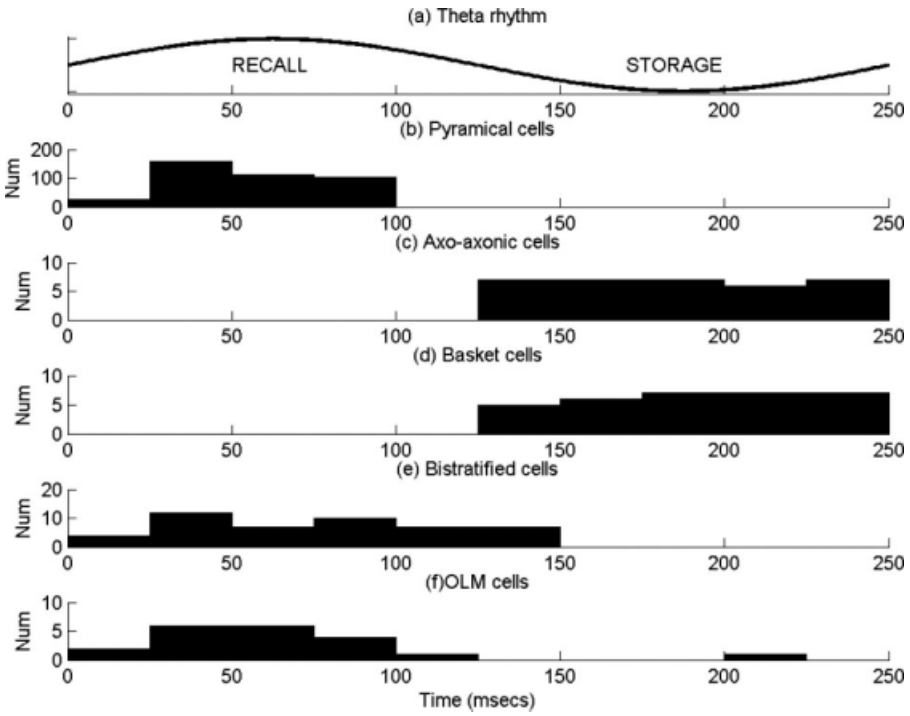

FIGURE 8. Simulated firing histograms of model cells with respect to extracellular theta oscillation. (a) Simulation theta oscillation as measured from the pyramidal layer of CA1. (b) Pyramidal cells (c) Axo-axonic cell. (d) Basket cells. (e) Bistratified cell. (f) OLM cells. Histograms were generated from cell spiking during runs of 8 theta cycles. Spike times were normalized to a theta cycle (250 ms) and binned into 10 ms bins.

Methods section, a set of patterns are stored without recourse to the STDP learning rule by generating a weight matrix based on a clipped Hebbian learning rule, and using the weight matrix to prespecify the CA3 to CA1 PC connection weights. To test recall of a previously stored pattern, the associated input pattern is applied as a cue in the form of spiking of active CA3 inputs (those belonging to the pattern) distributed within a gamma frequency time window. The entire cue pattern is repeated at gamma frequency (40 Hz; Fig. 4). At the same time, the 20 EC inputs also fire randomly distributed within a 25 ms gamma window, but with mean activity preceding the CA3 activity by 9 ms (Fig. 3). During storage and recall all inhibitory interneurons in the network switch on and off as it has been detailed in Storage and recall mechanism section. The CA3 spiking drives the CA1 PCs plus the B, AA, and BS interneurons. The EC input also drives the B and AA interneurons. To test pure recall by the CA3 input cue, in the following results the EC input is disconnected from the CA1 PCs. Also, STDP learning is switched off, but the CA3 synapses are still suppressed during the "storage" phase of theta. Pattern recall only occurs during the "recall" half-cycle. Typical firing patterns of the different cell types across a theta cycle are illustrated in Figure 8.

The recall of the first pattern in a set of five is shown in Figure 9. Subplots (a) and (b) are raster plots of the spiking of (a) septal (top 10 rows), EC (next 20 rows) and CA3 (bottom 100 rows) input and (b) CA1 PCs, respectively. The CA1 PCs are active two or three times during a recall cycle, with their spiking activity being a very close match to the stored pattern. Seven recall cycles are shown, following an initialization period of 200 ms.

Recall performance is calculated by measuring the CA1 PC spiking activity during a sliding 10 ms time window (Fig. 9c shows spike counts in each time window). For each window a binary vector of length 100 is formed, with entries having a value of 1 if the corresponding PC spikes in the window. The correlation [normalized dot product; Eq. (5)] of this vector with the expected pattern vector is calculated to give a measure of recall quality between 0 and 1, with 1 corresponding to perfect recall. Figure 9d shows recall quality over time. When CA1 PC spiking occurs, always the first PCs to fire are the ones belonging to the stored pattern, and quality goes to one. This is sometimes quickly followed by the firing of a few spurious PCs and the quality drops (see recall events at 900, 1,350, and 1,850 ms). Most recall events in this example are perfect and the recall quality averages at 0.98 (Fig. 12). Figure 10 shows voltage traces from a CA1 PC that belongs to the pattern, plus each of the four classes of interneuron. The phase relationships of the interneuron firing can be seen.

So far, we have considered recall when EC input is not present. An EC input corresponding to the cued pattern could potentially aid recall. Figures 11a, b shows PC recall activity without (Fig. 11a) and with (Fig. 11b) contribution from EC input. With EC input, the pattern is nearly perfectly recalled on each gamma cycle during a recall theta half-cycle.

To test the influence of the inhibitory pathways on recall, different pathways are selectively removed. Bistratified cell inhi-

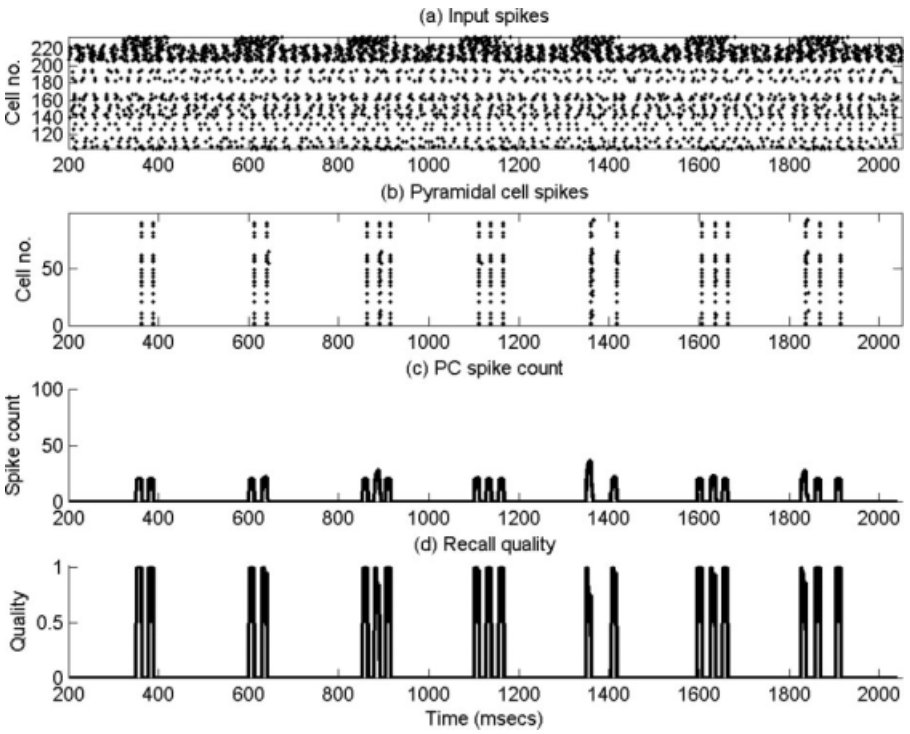

FIGURE 9. Example of pattern recall. The CA3 input is cueing the first pattern in a stored set of five. EC input is present to drive the inhibitory interneurons, but is disconnected from the CA1 Ps so that recall is due purely to the CA3 input cue. Seven 125 ms recall half-cycles are shown, starting at 300 ms (interspersed with 125 ms storage half-cycles, but STDP is turned off) (a) Raster plot showing the septal (top 10), EC (next 20) and CA3 input (bottom 100) spikes. (b) Raster plot showing CA1 P activity - virtually the only active cells are those belonging to the stored pattern. (c) P spike count in a sliding 10 ms bin. (d) Recall quality in a sliding 10 ms bin.

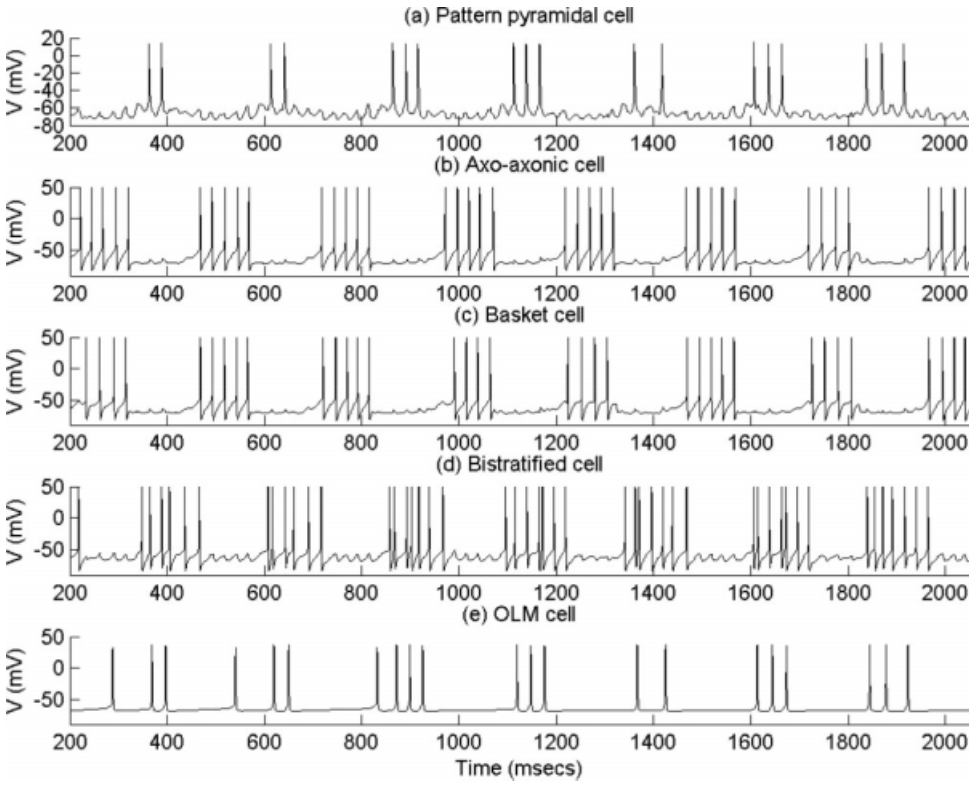

FIGURE 10. Voltage traces in an example of a P belonging to the pattern, and each type of inhibitory interneuron, for the recall episodes shown in Figure 9.

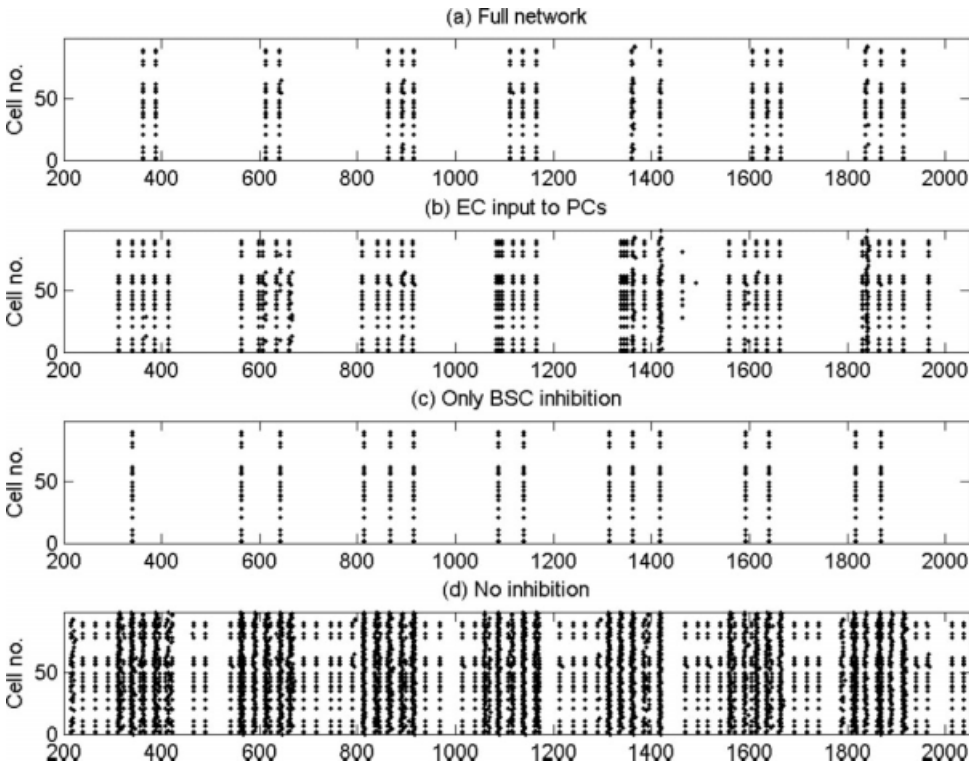

FIGURE 11. Raster plots of P activity during the same recall episodes as for Figure 9. (a) Same network configuration as in Figure 9, with EC input disconnected from Ps. (b) EC input now connected to Ps, so provides some recall cueing. (c) B and AA inhibition removed, so that recall is mediated only by BS inhibition (EC disconnected from Ps). (d) BS inhibition also removed.

bition to the medial SR PC dendrites is hypothesized to mediate thresholding of PC firing during recall. Removal of BC and AAC inhibition does not spoil recall quality, in accord with this hypothesis (Fig. 11c, 12). Removal of all inhibitory pathways leads to gamma frequency firing of virtually all PCs during recall cycles and the EC cued pattern during recall cycles (Fig. 11d). The average recall quality of each of these network configurations is shown in Figure 12. Average quality when all inhibition is removed is artificially high as EC input during storage cycles in now sufficient to overcome CA3 input suppression and fire only the pattern PCs, giving a false "high" recall quality during storage cycles.

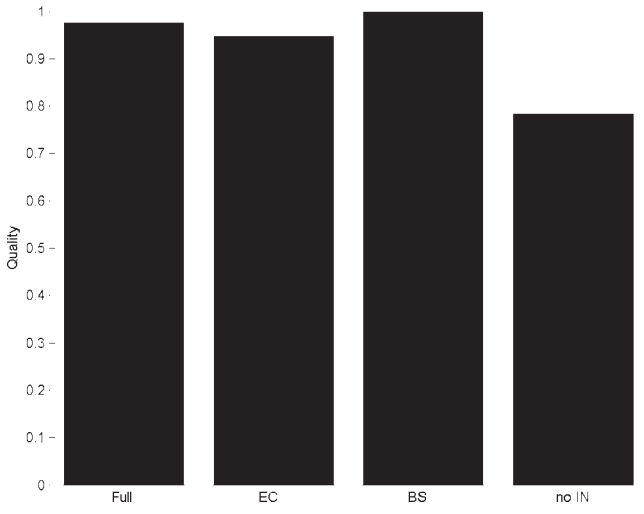

FIGURE 12. Average recall quality (measured over times when quality is nonzero) for the four network configurations shown in Figure 11.

OLM inhibition is hypothesized to remove interference from spurious EC input during recall. To test this, the EC input is now applied to the CA1 PCs throughout the theta cycle, but this input is taken to be due to a different pattern from that of the CA3 input cue i.e., CA1 PCs receiving the EC input may or may not belong to the cued pattern. Recall in this situation, with and without OLM inhibition to the SLM PC dendrites is shown in Figure 13. Recall is disrupted by the spurious EC input, but this disruption is significantly worse if the OLM inhibition is absent.

As is expected, average recall quality degrades when too many patterns are stored as PCs receive more excitation from cue patterns they do not belong to, leading to spurious firing. Figure 14 shows the mean recall quality as the number of stored patterns is increased.

Storage and Recall Performance

Now, we consider the storage and recall of new patterns via the STDP learning rule. In the model, storage and recall of memories is separated into two functional subcycles of each theta cycle (Hasselmo et al., 2002). The duration of a theta cycle was set to 250 ms (125 ms for storage and 125 ms for recall). Pattern presentation occurs at gamma frequency throughout theta, as described above. Now the EC and CA3

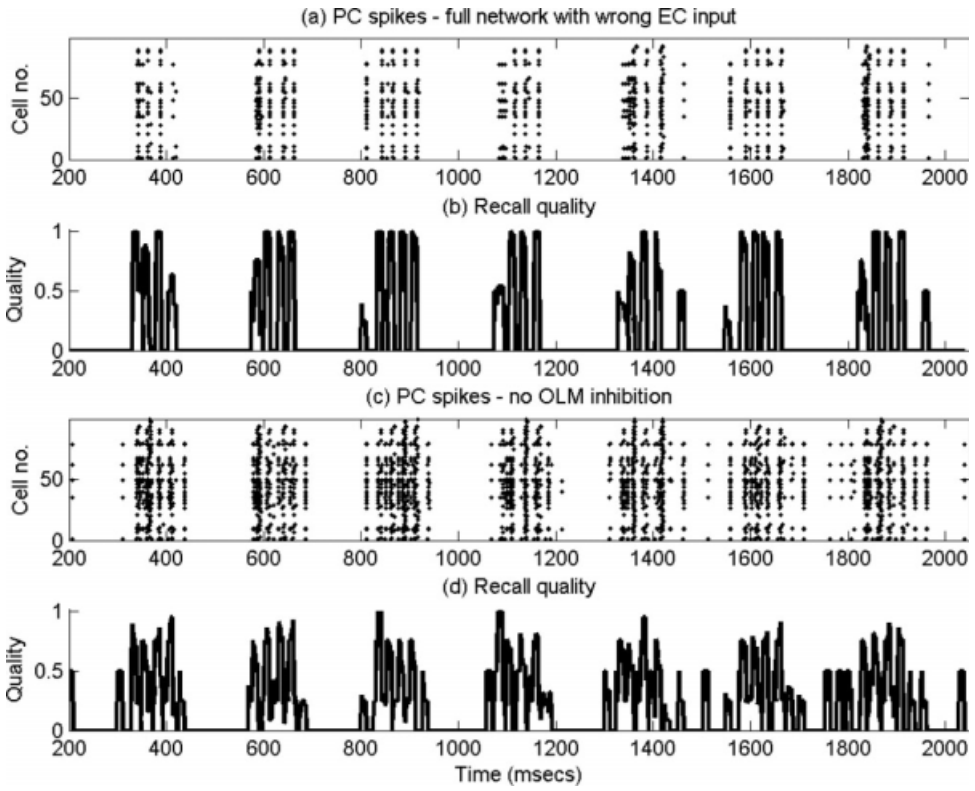

FIGURE 13. Pattern recall when recall is cued by the CA3 input, but EC input due to a different, spurious pattern is present on Ps. (a) Raster plot of P activity with full network. (b) Recall quality for (a). (c) P activity when OLM inhibition is removed. (d) Recall quality for (c).

inputs correspond to the output and input patterns, respectively, that are associated by modifying the CA3 AMPA synapses on the SR dendrites of CA1 PCs. EC input to PCs summating with CA3 input, provides the postsynaptic signal which is compared with the presynaptic spike times of CA3 inputs in the SR dendrites to drive the STDP learning rule. If the postsynaptic signal occurs a suitably short time after a presynaptic spike, the corresponding synapse is strengthened. If the signal is just before the presynaptic spike, the synapse is weakened.

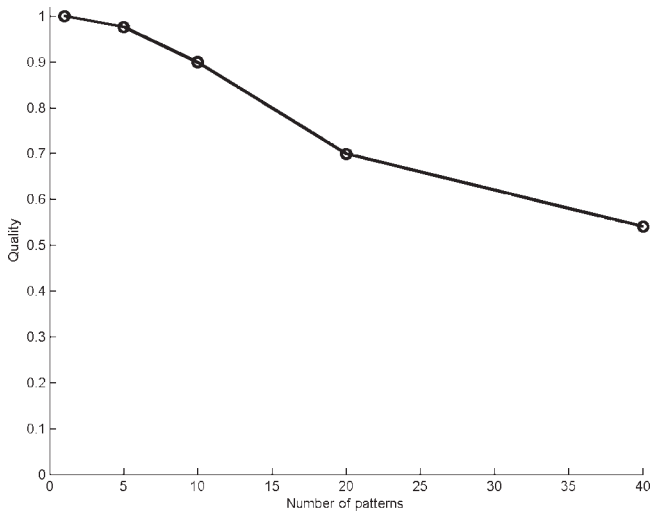

FIGURE 14. Average recall quality when recall is cued by CA3 input alone, for the full network, as a function of the number of stored patterns. Recall drops with a larger number of patterns due to an increase in spurious P activity. Note that the possible minimum quality when all cells become active is 0.4472.

Figure 15 shows storage of a new pattern by STDP learning. Storage can take place over four theta cycles, then the EC input is switched off. The remaining four theta cycles show recall of the newly stored pattern. Initially five patterns have already been stored by imposing the same predefined weight matrix as used in the recall experiments, above. If no learning takes place and the new pattern is used as a recall cue, then recall is basically absent, as expected (Fig. 15a). If pure LTP learning is used (plasticity factors $P = 1$ and $d = 0$), then the pattern is learnt perfectly over the four storage cycles (Fig. 15b). Inclusion of LTD disrupts learning (Fig. 15c). For this storage paradigm, LTD is unhelpful as learning a new pattern only requires strengthening the associated connections between those CA3 and CA1 PCs in the pattern. However, due to the timing of CA3 inputs relative to the peak PC response to EC input, LTD may occur.

Interference from previously stored patterns also may disrupt learning of a new pattern. If suppression of the CA3 inputs is removed during storage, then PCs outwith the new pattern may receive sufficient excitation from their CA3 input alone that LTP occurs at their CA3 synapses. This is shown in Figure 15d, where over twice as many PCs as are in the new pattern are now active during recall. Average recall quality for all these different cases is shown in Figure 16.

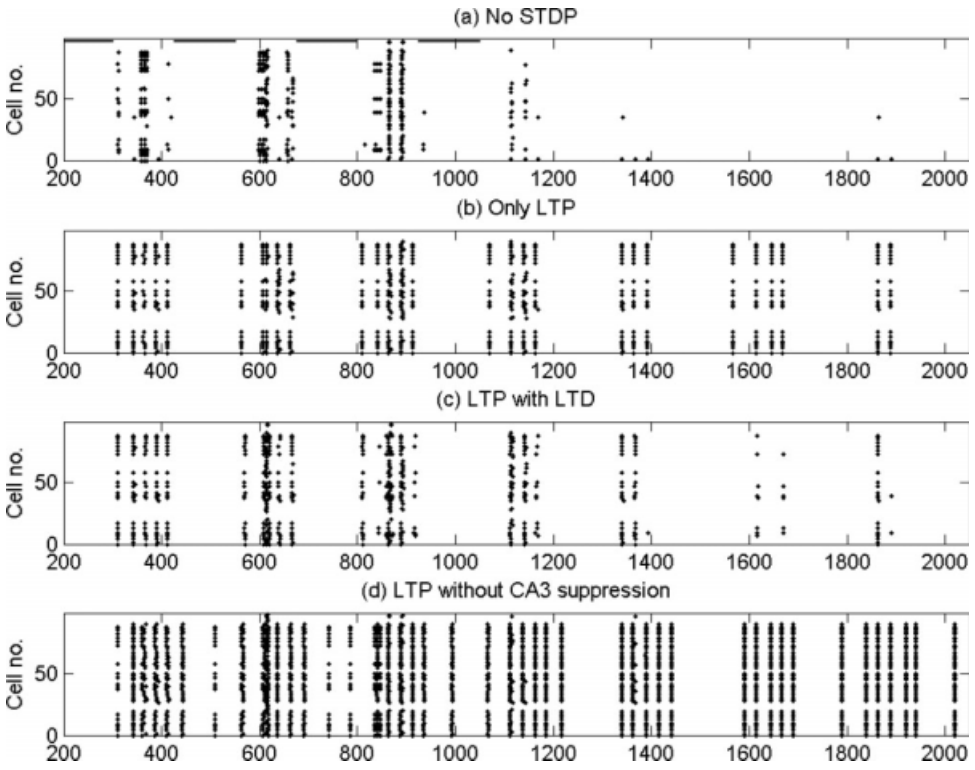

FIGURE 15. Storage of a new pattern, in addition to five previously stored patterns. To show the success or otherwise of storage, the EC input that drives storage is present only for four theta cycles (shown by the black horizontal lines at the top of (a)), then is switched off so that the final four cycles show recall of the newly stored pattern. (a) STDP is off, so no storage occurs. (b) Pure LTP during storage. (c) LTP plus a moderate amount of LTD. (d) LTP only, but without suppression of the CA3 input during storage cycles.

DISCUSSION

General Issues

A detailed biophysical model of the hippocampal CA1 microcircuitry has been presented, which demonstrates the biological feasibility of the separation of storage and recall processes into separate theta subcycles. The model simulated the timing of firing of different hippocampal cell types relative to the theta rhythm in anesthetized animals (Klausberger et al., 2003, 2004; Somogyi and Klausberger, 2005). The model proposed functional roles for different classes of inhibitory interneurons in encoding and retrieval of information. As others before (Kunec et al., 2005), it emphasized the cooperation of extra-hippocampal inputs for the proper memory storage and recall.

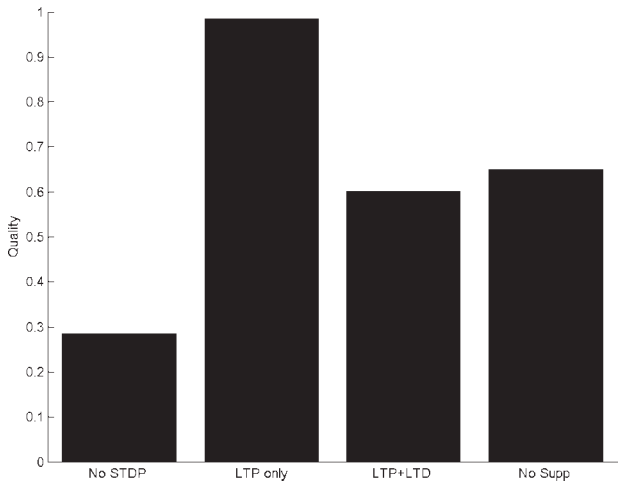

FIGURE 16. Average recall quality (measured over the final four theta cycles) for the four storage scenarios shown in Figure 15.

Model Predictions

In accordance with the data and models of Hasselmo et al. (Hasselmo et al., 1995; Wallenstein and Hasselmo, 1997; Molyneaux and Hasselmo, 2002), our model clearly demonstrates that during storage, suppression of feedforward CA3 synaptic input to CA1 is required to prevent interference from previously stored associations leading to excessive weight strengthening (Fig. 15). An additional mechanism is the B and AA inhibition, which during storage contributes to hyperpolarizing pattern and nonpattern pyramidal cells and hence prevents the former from firing and information from "leaking out" and the latter from learning the pattern.

An equally important prediction is that the STDP rule can store a new pattern, as determined by EC inputs, in association

with a CA3 input pattern provided (a) EC and CA3 inputs are repeatedly presented such that the "next" EC input arrives within the STDP LTP time window following a CA3 input, and (b) LTD is not too strong since, due to transmission delays, an EC input will always arrive within the STDP LTD time window preceding a CA3 input (based on the assumption that the layer II and layer III EC cells fire in phase with each other).

Finally, our model predicts that during recall, inhibition from BSCs is needed for accurate recall of a previously stored pattern by contributing to the thresholding of pyramidal cell firing, whereas OLM inhibition is effective at removing spurious EC input that may distort pattern recall.

Comparison With Other Models

Several computational network models of hippocampal dynamics of storage and recall have been advanced over the years (Hasselmo and Schnell, 1994; Treves and Rolls, 1992, 1994; Hasselmo et al., 1995; Hasselmo et al., 1996; Levy, 1996; Wallenstein and Hasselmo, 1997; Sommer and Wennekers, 2000, 2001; Hasselmo and Fehlau, 2001; Hasselmo et al., 2002; Kunec et al., 2005; Cutsuridis et al., 2007; Graham and Cutsuridis, 2009; Cutsuridis and Wennekers, in press). Here, we will focus only on those studies that developed network models of both excitatory and inhibitory neurons and proposed functional roles for different classes of inhibitory interneurons in the storage and recall processes. Menschik and Finkel (1998) advanced a network model of hippocampal CA3 region dynamics inspired by the Buzsaki "two-stage" memory model and his suggested role for interneurons (Buszaki, 1989; Buzsaki and Chrobak, 1995) and the Lisman et al. model on embedded gamma cycles within the theta rhythm (Lisman and Idiart, 1995; Lisman, 2005). Menschik and Finkel (1998) used detailed biophysical representations of multi-compartmental models of pyramidal cells and two types of inhibitory interneurons: basket cells and axoaxonic cells to study the modulation and control of storage and recall dynamics in Alzheimer's disease by subcortical cholinergic and GABAergic input to the hippocampus. Their results supported the hypothesis that spiking and bursting in CA3 pyramidal cells mediate separate behavioral functions and that cholinergic input regulates the transition between behavioral states associated with the online processing and recall of information. Cholinergic deprivation led to the slowing of gamma frequency, which reduced the number of "gamma cycles" within the theta rhythm available to reach the desired attractor state (i.e., memory loss and cognitive slowing seen in AD). Despite the model's successes, it had several limitations. Firstly, it did not assign distinct roles to basket cells and axoaxonic cells during the encoding and retrieval processes. Secondly, it assumed that the GABAergic synapses on pyramidal cells were plastic, a feature that hasn't been verified experimentally. Thirdly, Hasselmo and Fehlau (2001) showed that cholinergic effects occur on a slower timescale than the theta frequency, and hence its role in encoding and retrieval of information is seriously doubted.

Our research differs from this model in several ways, but shares several features with the Kunec et al. (2005) model of the CA3 mircocircuit, though ours is a network model of the CA1 microcircuitry. Firstly, as in Kunec et al. (2005), we adopted the Hasselmo et al. (2002) hypothesis that storage and recall in CA1 are separated into functionally independent subcycles embedded in the theta rhythm. This way, our network switched between modes of operation within the same learning task.

Secondly, our model uses detailed biophysical representations of multi-compartmental models of not only pyramidal cells, but, for the first time, of four different types of inhibitory interneurons found in the CA1 microcircuitry. All neurons in the model adopted their morphologies from experimental data and used a wealth of intrinsic currents in their dendritic compartments that affected action potential timing, which was crucial in P cells for synaptic plasticity.

Thirdly, all four inhibitory interneurons have specific functional roles during the encoding and retrieval processes (Klausberger et al. 2003, 2004; Somogyi and Klausberger, 2005). We propose that in our CA1 microcircuit model the basket and axo-axonic cells prevent pyramidal cells from firing during the encoding process, but also set the stage for learning to occur. During the retrieval process, bistratified cells set the threshold for pyramidal neurons so that those that had not learnt the pattern were silent, whereas those that had to be able to reliably recall it were active. OLM cells helped prevent errors and facilitate disambiguation during the retrieval (Kunec et al., 2005). The firing phases of the all neurons in our model were modulated by the θ-driven inhibition from the septal region (Kunec et al., 2005).

Finally, most of the previous models relied on Hebbian synaptic plasticity. In our model, encoding occurred based on a local STDP learning rule in P cell SR dendrites between the EC and CA3 inputs. As in Kunec et al. (2005), for our plasticity to occur, the postsynaptic neuron did not have to produce an action potential, but simply needed a depolarized dendritic membrane potential to elicit the strengthening process (Golding et al., 2002).

Model Extensions and Alternatives

These analyses show that the input pattern presentation period has a serious effect on the recall performance of our model at different levels of pattern loading. Several extensions to the basic idea deserve further consideration. It has been known for some time that the SR synapses of the CA1 pyramidal cells are surprisingly unreliable at signaling the arrival of single presynaptic action potentials to the postsynaptic neuron. On the other hand, bursts are reliably signaled, because transmitter release is facilitated. In the hippocampus, a single burst can produce long-term synaptic modifications (Allen and Stevens, 1994). Lisman (1997) has indicated that bursts signal the slope of synaptic input in contrast to simple cell firing, which signals how far the input is above the threshold, irrespective of slope. Work is underway in our laboratory to examine more

thoroughly the effects of bursts on the local STDP learning rule of a single CA1 pyramidal neuron as well as on the storage and recall of our CA1 microcircuit network. Special emphasis will be given on how the firing of the inhibitory interneurons changes in the presence of bursts and whether their timing changes relative to theta rhythm.

Also, we are testing the performance of our network using a more biophysical description of the STDP learning rule (Rubin et al., 2005; Cutsuridis et al., 2008b). Simulation results of a reduced single P cell CA^{2+} dynamics model of STDP in the presence of GABA-A inhibition at its proximal SR dendrites (Cutsuridis et al., 2008b; Cutsuridis et al., in press) replicated the experimentally observed asymmetry-to-symmetry transition in the SR dendrites. The model predicted that gamma frequency inhibition is a necessary condition for the transition in the CA1-SR dendrites, the transition is dependent on the conductance value of GABA-A, the relative timing between the GABA inhibition and the excitatory pair, the LTP peak of the symmetric STDP curve is centered at 10 ms and the two LTD windows are evident at −10 ms and +40 ms (Cutsuridis et al., 2008b; Cutsuridis et al., 2009). Simulation results of the same model (Cutsuridis et al., in press) replicate all experimental evidence in the presence of triplets and quadruplets (Wang et al., 2005).

The hypotheses and model presented above are still very simple compared with what we know of the CA1 microcircuit. More cell types and their connectivity could be included in the model. However, we still require further data on type-specific cell properties and their in vivo firing patterns. In our model, only the synapses on the SR dendrites of P cells are modifiable. In reality, however, most, if not all synaptic pathways are modifiable in the face of particular patterns of activity. For example, the entorhinal input to the distal dendrites of CA1 P cells is Hebbian modifiable, and the postsynaptic signals in these dendrites is under specific inhibitory and neuromodulatory control (Remondes and Schuman, 2002; Judge and Hasselmo, 2004). Computational CA1 models clearly need to take into account more aspects of this pathway (Pissadaki and Poirazi, 2007), in particular what learning may take place. Finally, the excitatory synapses on the inhibitory interneurons may be plastic and hence the INs can be a part of smaller circuits within the global CA1 microcircuit capable of carrying out specific functionalities, such as ensuring the reliability of recall of the input pattern for all time windows (gamma cycles) of recall.

REFERENCES

Allen C, Stevens CF. 1994. An evaluation of causes for unreliability of synaptic transmission. Proc Natl Acad Sci USA 91:10380–10383.

Amaral D, Lavenex P. 2007. Hippocampal neuroanatomy. In: Andersen P, Morris R, Amaral D, Bliss T, O'Keefe J, editors. The Hippocampus Book. Oxford: University Press. pp 37–114.

Amit DJ. 1989. Modeling Brain Function: The World of Attractor Neural Networks. New York: Cambridge University Press.

Andersen P, Morris R, Amaral D, Bliss T, O'Keefe J. 2007. The Hippocampus Book. Oxford: University Press.

Ault B, Nadler JV. 1982. Baclofen selectively inhibits transmission at synapses made by axons of CA3 pyramidal cells in the hippocampal slice. J Pharmcol Exp Ther 223:291–297.

Axmacher N, Morman F, Fernandez G, Elger C, Fell J. 2006. Memory formation by neuronal synchronization. Brain Res Rev 52:170–182.

Brankack J, Stewart M, Fox S. 1993. Current source density analysis of the hippocampal theta rhythm: Associated sustained potentials and candidate synaptic generators. Brain Res 615:310–327.

Brun VH, Otnass MK, Molden S, Steffenach HA, Witter MP, Moser MB, Moser EI. 2002. Place cells and place recognition maintained by direct entorhinal-hippocampal circuitry. Science 296:2243–2246.

Buckingham J, Willshaw D. 1993. On setting unit thresholds in an incompletely connected associative net. Network 4:441–459.

Buhl EH, Halasy K, Somogyi P. 1994a. Diverse sources of hippocampal unitary inhibitory postsynaptic potentials and the number of synaptic release sites. Nature 368:823–828.

Buzsaki G. 1989. Two-stage model of memory trace formation: A role for "noisy" brain states. Neuroscience 31:551–570.

Buzsaki G. 2002. Theta oscillations in the hippocampus. Neuron 33:325–340.

Buzsaki G, Chrobak JJ. 1995. Temporal structure in spatially organized neuronal assembles: A role for interneuronal networks. Curr Opin Neurobiol 5:504–510.

Cobb SR, Buhl EH, Halasy K, Paulsen O, Somogyi P. 1995. Synchronization of neuronal activity in hippocampus by individual GABAergic interneurons. Nature 378:75–78.

Colbert CM, Levy WB. 1992. Electrophysiological and pharmacological characterization of perforant path synapses in CA1: Mediation by glutamate receptors. J Neurophysiol 68:1–7.

Cutsuridis V, Wenneckers T. Hippocampus, microcircuits and associative memory. Neural Netw (in press).

Cutsuridis V, Hunter R, Cobb S, Graham BP. 2007. Storage and recall in the CA1 microcircuit of the hippocampus: A biophysical model. In: 16th Annual Computational Neuroscience Meeting CNS*2007, Toronto, Canada, July 8th–12th. BMC Neurosci 8(suppl 2):P33.

Cutsuridis V, Cobb S, Graham BP. 2008a. Encoding and retrieval in a CA1 microcircuit model of the hippocampus. In: 18th International Conference on Artificial Neural Networks, LNCS Vol. 5164. Berlin/Heidelberg: Springer, Sept. 3–6, 2008, Prague, Czech Republic. pp 238–247.

Cutsuridis V, Cobb S, Graham BP. 2008b. A Ca^{2+} dynamics model of the STDP symmetry-to-asymmetry transition in the CA1Pyramidal cell of the hippocampus. In: 18th International Conference on Artificial Neural Networks, LNCS Vol. 5164. Berlin/Heidelberg: Springer, Sept. 3–6, 2008, Prague, Czech Republic. pp 627–635.

Cutsuridis V, Cobb S, Graham BP. 2008c. A CA1 heteroassociative microcircuit model of the hippocampus. In: ARIADNE: Research in Encoding and Decoding of Neural Ensembles, Santorini, Greece, June 26–29.

Cutsuridis V, Graham BP, Cobb S. 2009. Modelling the effects of GABA-A inhibition on the spike timing dependent plasticity (STDP) of a CA1 pyramidal cell. In: 18th Annual Computational Neuroscience Meeting CNS*2009, Berlin, Germany, July 17th–23rd.

Cutsuridis V, Cobb S, Graham BP. Modelling the STDP symmetry-to-asymmetry transition in the presence of GABAergic inhibition. Neural Netw World (in press).

Eichenbaum H, Dunchenko P, Wood E, Shapiro M, Tanila H. 1999. The hippocampus, memory and place cells: Is it spatial memory or a memory of space? Neuron 23:209–226.

Freund TF, Buzsaki G. 1996. Interneurons of the hippocampus. Hippocampus 6:347–470.

Ganter P, Szucs P, Paulsen O, Somogyi P. 2004. Properties of horizontal axo-axonic cells in stratum oriens of the hippocampal CA1 area of rats in vitro. Hippocampus 14:232–243.

Golding NL, Staff N, Spruston N. 2002. Dendritic spikes as a mechanism for cooperative long-term potentiation. Nature 418:326–331.

Golding NL, Mickus TJ, Katz Y, Kath WL, Spruston N. 2005. Factors mediating powerful voltage attenuation along CA1 pyramidal neuron dendrites. J Physiol 568:69–82.

Graham B, Willshaw D. 1995. Improving recall from an associative memory. Biol Cybern 72:337–346.

Graham B, Willshaw D. 1997. Capacity and information efficiency of the associative net. Network 8:35–54.

Graham B, Willshaw D. 1999. Probabilistic synaptic transmission in the associative net. Neural Comp 11:117–137.

Graham BP, Cutsuridis V. 2009. Dynamical information processing in the CA1 microcircuit of the hippocampus. In: Heinke D, Mavritsaki E, editors. Computational Modelling in Behavioural Neuroscience: Closing the Gap Between Neurophysiology and Behavior. London: Psychology Press, Taylor and Francis Group.

Hasselmo ME, Schnell E. 1994. Laminar selectivity of the cholinergic suppression of synaptic transmission in rat hippocampal region CA1: Computational modeling and brain slice physiology. J Neurosci 14:3898–3914.

Hasselmo M, Fehlau B. 2001. Differences in the time course of Ach and GABA modulation of excitatory synaptic potentials in the slice of rat hippocampus. J Neurophysiol 86:1792–1802.

Hasselmo ME, Schnell E, Barkai E. 1995. Dynamics of learning and recall at excitatory recurrent synapses and cholinergic modulation in rat hippocampal region CA3. J Neurosci 15:5249–5262.

Hasselmo ME, Wyble BP, Wallenstein GV. 1996. Encoding and retrieval of episodic memories: Role of cholinergic and GABAergic modulation in the hippocampus. Hippocampus 6:693–708.

Hasselmo M, Bodelon C, Wyble B. 2002. A proposed function of the hippocampal theta rhythm: Separate phases of encoding and retrieval of prior learning. Neural Comput 14:793–817.

Hines ML, Carnevale T. 1997. The NEURON simulation environment. Neural Comput 9:1179–1209.

Hopfield J. 1982. Neural networks and physical systems with emergent collective computational abilities. Proc Natl Acad Sci USA 79:2554–2558.

Jensen O, Lisman J. 1996. Novel lists of 7 +/− known items can be reliably stored in a oscillatory short-term memory network: interaction with long-term memory. Learn Mem 3(2–3):257–263.

Judge SJ, Hasselmo ME. 2004. Theta rhythmic stimulation of stratum lacunosum-moleculare in rat hippocampus contributes to associative LTP at a phase offset in stratum radiatum. J Neurophysiol 92:1615–1624.

Klausberger T, Magill PJ, Marton LF, David J, Roberts B, Cobden PM, Buzsaki G, Somogyi P. 2003. Brain-state- and cell-type-specific firing of hippocampal interneurons in vivo. Nature 421:844–848.

Klausberger T, Marton LF, Baude A, Roberts JD, Magill PJ, Somogyi P. 2004. Spike timing of dendrite-targeting bistratified cells during hippocampal network oscillations in vivo. Nat Neurosci 7:41–47.

Kunec S, Hasselmo ME, Kopell N. 2005. Encoding and retrieval in the CA3 region of the hippocampus: A model of theta-phase separation. J Neurophysiol 94:70–82.

Leung LS, Roth L, Canning KJ. 1995. Entorhinal inputs to hippocampal CA1 and dentate gyrus in the rat: A current-source-density study. J Neurophysiol 73:2392–2403.

Levy W. 1996. A sequence predicting CA3 is a flexible associator that learns and uses context to solve hippocampal-like tasks. Hippocampus 6:579–590.

Lisman J. 1997. Bursts as a unit of neural information: Making unreliable synapses reliable. Trends Neurosci 20:38–43.

Lisman J. 2005. The theta/gamma discrete phase code occurring during the hippocampal phase precession may be a more general brain coding scheme. Hippocampus 15:913–922.

Lisman J, Idiart MA. 1995. Storage of 7±2 short-term memories in oscillatory subcycles. Science 267:1512–1515.

Magee JC, Cook EP. 2000. Somatic EPSP amplitude is independent of synapse location in hippocampal pyramidal neurons. Nature 3:895–903.

Menschik ED, Finkel LH. 1998. Neuromodulatory control of hippocampal function: Towards a model of Alzheimer's disease. Artif Intell Med 13:99–121.

Moczydlowski E, Latorre R. 1983. Gating kinetics of Ca2+-activated K+ channels from rat muscle incorporated into planar lipid bilayers. J Gen Physiol 82:511–542.

Molyneaux BJ, Hasselmo ME. 2002. $GABA_B$ presynaptic inhibition has an in vivo time constant sufficiently rapid to allow modulation at theta frequency. J Neurophysiol 87:1196–1205.

Paulsen O, Moser E. 1998. A model of hippocampal memory encoding and retrieval: GABAergic control of synaptic plasticity. Trends Neurosci 21:273–279.

Petersen CCH, Malenka RC, Nicoll RA, Hopfield JJ. 1998. All-or-none potentiation at CA3-CA1 synapses. Proc Natl Acad Sci USA 95:4732–4737.

Pissadaki E, Poirazi P. 2007. Modulation of excitability in CA1 pyramidal neurons via the interplay of entorhinal cortex and CA3 inputs. Neurocomputing 70:1735–1740.

Poirazzi P, Brannon T, Mel BW. 2003a. Arithmetic of subthreshold synaptic summation in a model CA1 pyramidal cell. Neuron 37:977–987.

Poirazzi P, Brannon T, Mel BW. 2003b. Pyramidal neuron as a 2-layer neural network. Neuron 37:989–999.

Remondes M, Schuman E. 2002. Direct cortical input modulates plasticity and spiking in CA1 pyramidal neurons. Nature 416:736–740.

Rubin JE, Gerkin RC, Bi GQ, Chow CC. 2005. Calcium time course as signal for spike-timing-dependent plasticity. J Neurophysiol 93:2600–2613.

Santhakumar V, Aradi I, Soltetz I. 2005. Role of mossy fiber sprouting and mossy cell loss in hyperexcitability: A network model of the dentate gyrus incorporating cells types and axonal topography. J Neurophysiol 93:437–453.

Saraga F, Wu CP, Zhang L, Skinner FK. 2003. Active dendrites and spike propagation in multicompartmental models of oriens-lacunosum/moleculare hippocampal interneurons. J Physiol 552:673–689.

Soleng AF, Raastad M, Andersen P. 2003. Conduction latency along CA3 hippocampal axons from rat. Hippocampus 13:953–961.

Sommer FT, Wennekers T. 2000. Modelling studies on the computational function of fast temporal structure in cortical circuit activity. J Physiol (Paris) 94:473–488.

Sommer FT, Wennekers T. 2001. Associative memory in networks of spiking neurons. Neural Netw 14:825–834.

Somogyi P, Klausberger T. 2005. Defined types of cortical interneurons structure space and spike timing in the hippocampus. J Physiol 562:9–26.

Stewart M, Fox S. 1990. Do septal neurons pace the hippocampal theta rhythm? Trends Neurosci 13:163–169.

Stuart G, Spruston N. 1998. Determinants of voltage attenuation in neocortical pyramidal neuron dendrites. J Neurosci 18:3501–3510.

Traub R, Jefferys J, Whittington M. 1999. Fast oscillations in cortical circuits. Cambridge, Massachusetts: MIT Press.

Treves A, Rolls E. 1992. Computational constraints suggest the need for two distinct input systems to the hippocampal CA3 network. Hippocampus 2:189–200.

Treves A, Rolls E. 1994. Computational analysis of the role of the hippocampus in memory. Hippocampus 4:374–391.

Wallenstein GV, Hasselmo ME. 1997. GABArgic modulation of hippocampal population activity: Sequence learning, place field development and the phase precession effect. J Neurophysiol 78: 393–408.

Wang HX, Gerkin RC, Nauen DW, Bi GQ. 2005. Coactivation and timing-dependent integration of synaptic potentiation and depression. Nat Neurosci 8:187–193.

Whittington M, Traub R. 2003. Inhibitory interneurons and network oscillations in vitro. Trends Neurosci 26:676–682.

Willshaw D, Buneman O, Longuet-Higgins H. 1969. Non-holographic associative memory. Nature 222:960–962.

Wood E, Dunchenko P, Eichenbaum H. 1999. The global record of memory in hippocampal neuronal activity. Nature 397:613–616.

Wyble BP, Linster C, Hasselmo ME. 2000. Size of CA1-evoked synaptic potentials is related to theta rhythm phase in rat hippocampus. J Neurophysiol 83:2138–2144.

APPENDIX: MATHEMATICAL FORMALISM

Pyramidal Cell

The somatic (s), axonic (a) and radiatum (rad), lacunosum-moleculare (LM) and oriens (ori) dendritic compartments obey the following current balance equations:

$$C\frac{dV_s}{dt} = -I_{\mathrm{L}} - I_{\mathrm{Na}} - I_{\mathrm{kdr}} - I_{\mathrm{A}} - I_{\mathrm{M}} - I_{\mathrm{h}} - I_{\mathrm{sAHP}} - I_{\mathrm{mAHP}} - I_{\mathrm{CaL}} - I_{\mathrm{CaT}} - I_{\mathrm{CaR}} - I_{\mathrm{buff}} - I_{\mathrm{syn}} \quad \text{(A1)}$$

$$C\frac{dV_a}{dt} = -I_{\mathrm{L}} - I_{\mathrm{Na}} - I_{\mathrm{kdr}} - I_{\mathrm{M}} - I_{\mathrm{syn}} \quad \text{(A2)}$$

$$C\frac{dV_{\mathrm{rad,ori}}}{dt} = -I_{\mathrm{L}} - I_{\mathrm{Na}} - I_{\mathrm{kdr}} - I_{\mathrm{A}} - I_{\mathrm{M}} - I_{\mathrm{h}} - I_{\mathrm{sAHP}} - I_{\mathrm{mAHP}} - I_{\mathrm{CaL}} - I_{\mathrm{CaT}} - I_{\mathrm{CaR}} - I_{\mathrm{buff}} - I_{\mathrm{syn}} \quad \text{(A3)}$$

$$C\frac{dV_{\mathrm{LM}}}{dt} = -I_{\mathrm{L}} - I_{\mathrm{Na}} - I_{\mathrm{kdr}} - I_{\mathrm{A}} - I_{\mathrm{syn}} \quad \text{(A4)}$$

where I_{L} is the leak current, I_{Na} is the fast sodium current, I_{kdr} is the delayed rectifier potassium current, I_{A} is the A-type K^+ current, I_{M} is the M-type K^+ current, I_{h} is a hyperpolarizing h-type current, I_{CaL}, I_{CaT} and I_{CaR} are the L-, T- and R-type Ca^{2+} currents, respectively, I_{sAHP} and I_{mAHP} are slow and medium Ca^{2+} activated K^+ currents, I_{buff} is a calcium pump/buffering mechanism and I_{syn} is the synaptic current. The conductance and reversal potentials values for all ionic currents are listed in Table 2.

The sodium current is described by:

$$I_{\mathrm{Na}} = \bar{g}_{\mathrm{Na}} \times m^2 \times h \times s \times (V - E_{\mathrm{Na}}) \quad \text{(A5)}$$

where an additional variable '*s*' is introduced to account for dendritic location-dependent slow attenuation of the sodium current (Poirazzi et al., 2003a, b). Activation and inactivation kinetics for I_{Na} are given by:

$$m_{t+dt} = m_t + (1 + e^{-\frac{dt}{\tau_m}}) \times (m_{\mathrm{inf}} - m_t), \quad m_{\mathrm{inf}} = \frac{1}{1 + e^{(-\frac{V+40}{3})}}$$

$$h_{t+dt} = h_t + (1 - e^{-\frac{dt}{\tau_h}}) \times (h_{\mathrm{inf}} - h_t), \quad h_{\mathrm{inf}} = \frac{1}{1 + e^{(\frac{V+45}{3})}}$$

$$s_{t+dt} = s_t + (1 + e^{-\frac{dt}{\tau_\sigma}}) \times (s_{\mathrm{inf}} - s_t), \quad s_{\mathrm{inf}} = \frac{1 + Na_{att} \times e^{(\frac{V+60}{2})}}{1 + e^{(\frac{V+60}{2})}}$$

with $dt = 0.1\ ms$ and time constants $\tau_{\mathrm{m}} = 0.05$ ms, $\tau_{\mathrm{h}} = 0.5$ ms, and

$$\tau_\sigma = \frac{0.00333(\mathrm{ms}) \times e^{0.0024(1/mV) \times (V+60) \times Q(^\circ\mathrm{C})}}{1 + e^{0.0012(1/mV) \times (V+60) \times Q(^\circ\mathrm{C})}}$$

The function $Q(^\circ\mathrm{C})$ is given by:

$$Q(^\circ\mathrm{C}) = \frac{F}{R \times (T + ^\circ\mathrm{C})}$$

where $R = 8.315$ J/°C, $F = 9.648 \times 10^4$Coul, $T = 273.16$ in degrees Kelvin and °C is the temperature in degrees celsius. The $\mathrm{Na_{att}}$ variable represents the degree of sodium current attenuation and varies linearly from soma to distal trunk ($\mathrm{Na_{att}} \in [0 \rightarrow 1]$: maximum → zero attenuation). The delayed rectifier current is given by:

$$I_{\mathrm{Kdr}} = \bar{g}_{\mathrm{Kdr}} \times m^2 \times (V - E_K) \quad \text{(A6)}$$

$$m_{t+dt} = m_t + (1 - e^{-\frac{dt}{2.2}}) \times (m_{\mathrm{inf}} - m_t), \quad m_{\mathrm{inf}} = \frac{1}{1 + e^{(-\frac{V+42}{2})}}$$

The sodium and delayed rectifier channel properties are slightly different in the soma, axis and dendritic arbor. To fit experimental data regarding the backpropagation of spike trains, soma and axon compartments have a lower threshold for Na^+ spike initiation (≈−57 mV) than dendritic ones (≈−50 mV). Thus, the m_{inf} and h_{inf} somatic/axonic HH channel kinetics as well as the time constants for both $I^{\mathrm{sa}}_{\mathrm{Na}}$ and $I^{\mathrm{sa}}_{\mathrm{Kdr}}$, are modified as follows. For the sodium

$$m^{\mathrm{sa}}_{\mathrm{inf}} = \frac{1}{1 + e^{(-\frac{V+44}{3})}}, \quad h^{\mathrm{sa}}_{\mathrm{inf}} = \frac{1}{1 + e^{(\frac{V+49}{3.5})}}$$

while for the potassium delayed rectifier

$$m^{\mathrm{sa}}_{\mathrm{inf}} = \frac{1}{1 + e^{(-\frac{V+46.3}{3})}}$$

The somatic time constant for somatic/axonic Na^+ channel activation is kept the same $\tau_{\mathrm{m}} = 0.05$ ms while for inactivation is set to $\tau_{\mathrm{h}} = 1$ ms. The τ value for the delayed rectifier chan-

nel activation is set to $\tau_m = 3.5$ ms. In all of the following equations, τ values are given in ms.

The fast inactivating A-type K^+ current is described by

$$I_{\acute{A}} = \bar{g}_A \times n_A \times l \times (V - E_K) \tag{A7}$$

$$n_A(t+1) = n_A(t) + (n_{A_\infty} - n_A(t)) \times (1 - e^{-dt/\tau_n}),$$
$$\text{where } \tau_n = 0.2\ ms$$

$$n_{A_\infty} = \frac{\alpha_{n_A}}{\alpha_{n_A} + \beta_{n_A}}$$

$$\alpha_{n_A} = \frac{-0.01(V+21.3)}{e^{-(V+21.3)/35} - 1}, \quad \beta_{n_A} = \frac{0.01(V+21.3)}{e^{(V+21.3)/35} - 1}$$

$$l(t+1) = l(t) + (l_\infty - l(t)) \times (1 - e^{-dt/\tau_l})$$

$$l_\infty = \frac{\alpha_l}{\alpha_l + \beta l}$$

$$\alpha_l = \frac{-0.01(V+58)}{e^{(V+58)/8.2} - 1}, \quad \beta_l = \frac{0.01(V+58)}{e^{-(V+58)/8.2} - 1}$$

where $\tau_l = 5 + 26(V + 20)/10$, if $V > 20\ mV$ and $\tau_l = 5$, elsewhere.

The hyperpolarizing h-current is given by

$$I_h = g_h \times tt \times (V - E_h) \tag{A8}$$

$$\frac{dtt}{dt} = \frac{tt_\infty - tt}{\tau_{tt}}$$

$$tt_\infty = \frac{1}{1 + e^{-(V - V_{\text{half}})/k_l}},$$
$$\tau_{tt} = \frac{e^{0.0378 \times \varsigma \times \text{gmt} \times (V - V_{\text{halft}})}}{qtl \times q10^{(T-33)/10} \times a0t \times (1 + a_{tt})}$$

$$a_{tt} = e^{0.00378 \times \varsigma \times (V - V_{\text{halft}})}$$

where ζ, gmt, $q10$, and qtl are 2.2, 0.4, 4.5, and 1, respectively, $a0t$ is 0.0111 1/ms, $V_{\text{halft}} = -75$ mV and $k_l = -8$.

The slowly activating voltage-dependent potassium current, I_M, is given by the equations:

$$I_m = 10^{-4} \times T_{\text{adj}}(^\circ\text{C}) \times \bar{g}_m \times m \times (V - E_K) \tag{A9}$$

$$T_{\text{adj}}(^\circ\text{C}) = 2.3^{(^\circ\text{C}-23)/10}$$

$$m_{t+dt} = m_t + (1 - e^{-\frac{dt \times T_{\text{adj}}(^\circ\text{C})}{\tau}}) \times \left(\frac{\alpha(V)}{(\alpha(V) + \beta(V)} - m_t\right)$$

$$\alpha(V) = 10^{-3} \times \frac{(V+30)}{(1 - e^{-(V+30)/9})},$$
$$\beta(V) = -10^{-3} \times \frac{(V+30)}{(1 - e^{(V+30)/9})}, \quad \tau = \frac{1}{\alpha(V) + \beta(V)}$$

The slow after-hyperpolarizing current, I_{sAHP}, is given by:

$$I_{\text{sAHP}} = \bar{g}_{\text{sAHP}} \times m^3 \times (V - E_K) \tag{A10}$$

$$\frac{dm}{dt} = \frac{\frac{Cac}{(1+Cac)} - m}{\tau}$$

$$\tau = \max\left(\frac{1}{0.003(1/ms) \times (1 + Cac) \times 3^{(^\circ\text{C}-22)/10}}, 0.5\right)$$

where $Cac = (ca_{\text{in}}/0.025(mM))^2$.

The medium after-hyperpolarizing current, I_{mAHP} (Moczydlowski and Latorre, 1983), is given by:

$$\text{I}_{\text{mAHP}} = \bar{g}_{\text{mAHP}} \times m \times (V - E_K) \tag{A11}$$

$$m_{t+dt} = m_t + (1 + e^{-\frac{dt}{\tau_m}}) \times (\frac{\alpha_m(V)}{\tau_m} - m_t)$$

$$\alpha_m(V) = \frac{0.48(1/\text{ms})}{1 + \frac{0.18(mM)}{ca_{\text{in}}} \times e^{(-1.68 \times)V \times Q(^\circ\text{C}))}}$$

$$\beta_m(V) = \frac{0.28(1/\text{ms})}{1 + \frac{ca_{\text{in}}}{0.011(mM) \times e^{(-2 \times V \times Q(^\circ\text{C}))}}}$$

$$\tau_m = \frac{1}{\alpha_m(V) + \beta_m(V)}$$

The somatic high-voltage activated (HVA) L-type Ca^{2+} current is given by

$$I^s_{\text{CaL}} = \bar{g}^s_{\text{CaL}} \times m \times \frac{0.001\text{m}M}{0.001\text{m}M + ca_{\text{in}}} \times ghk(V, ca_{\text{in}}, ca_{\text{out}}) \tag{A12}$$

$$\alpha_m(V) = -0.055 \times \frac{(V+27.01)}{e^{-(V+27.01)/3.8} - 1},$$
$$\beta_m(V) = 0.94 \times e^{-(V+63.01)/17}$$

$$\tau_m = \frac{1}{5 \times (\alpha_m(V) + \beta_m(V))}$$

whereas the dendritic L-type calcium channels have different kinetics:

$$I^d_{\mathrm{CaL}} = \bar{g}^d_{\mathrm{CaL}} \times m^3 \times h \times (V - E_{\mathrm{Ca}}) \tag{A13}$$

$$\alpha(V) = \frac{1}{1 + e^{-(v+37)}}, \beta(V) = \frac{1}{1 + e^{(v+41)/0.5}}$$

Their time constants are equal to $\tau_m = 3.6\ ms$ and $\tau_h = 29\ ms$.

The low-voltage activated (LVA) T-type Ca^{2+} channel kinetics are given by:

$$I_{\mathrm{CaT}} = \bar{g}_{\mathrm{CaT}} \times m^2 \times h \frac{0.001mM}{0.001mM + ca_{\mathrm{in}}} \times ghk(V, ca_{\mathrm{in}}, ca_{\mathrm{out}}) \tag{A14}$$

$$ghk(V, ca_{\mathrm{in}}, ca_{\mathrm{out}}) = -x \times \left(1 - \frac{ca_{\mathrm{in}}}{ca_{\mathrm{out}}} \times e^{\frac{V}{x}}\right) \times f\left(\frac{V}{x}\right)$$

$$x = \frac{0.0853 \times (T + ^\circ\mathrm{C})}{2}, \quad f(z) = \begin{cases} 1 - \frac{z}{2} & \text{if abs(z)} < 10^{-4} \\ \frac{z}{e^z - 1} & \text{otherwise} \end{cases}$$

$$m_{t+dt} = m_t + (1 + e^{-\frac{dt}{\tau_m}}) \times \left(\frac{\alpha_m(V)}{\alpha_m(V) + \beta_m(V)} - m_t\right)$$

$$h_{t+dt} = h_t + (1 - e^{-\frac{dt}{\tau_h}}) \times \left(\frac{\alpha_h(V)}{\alpha_h(V) + \beta_h(V)} - h_t\right)$$

$$\alpha_m(V) = -0.196 \times \frac{(V - 19.88)}{e^{-(V-19.88)/10} - 1},$$
$$\beta_m(V) = 0.046 \times e^{-(V/22.73)}$$

$$\alpha_h(V) = 0.00016 \times e^{-(V+57)/19}, \ \beta_h(V) = \frac{1}{e^{-(V-15)/10} + 1}$$

$$\tau_m = \frac{1}{\alpha_m(V) + \beta_m(V)}, \tau_h = \frac{1}{0.68 \times (\alpha_h(V) + \beta_h(V))}$$

where ca_{in} and ca_{out} are the internal and external calcium concentrations. The HVA R-type Ca2+ current is described by:

$$I_{\mathrm{CaR}} = \bar{g}_{\mathrm{CaR}} \times m^3 \times h \times (V - E_{\mathrm{Ca}}) \tag{A15}$$

$$m_{t+dt} = m_t + (1 + e^{-\frac{dt}{\tau_m}}) \times (\alpha(V) - m_t)$$

$$h_{t+dt} = h_t + (1 - e^{-\frac{dt}{\tau_h}}) \times (\beta(V) - h_t)$$

The difference between somatic and dendritic CaR currents lies in the $\alpha(V)$, $\beta(V)$ and τ parameter values. For the somatic current, $\tau_m = 100$ ms and $\tau_h = 5$ ms while for the dendritic current $\tau_m = 50$ ms and $\tau_h = 5$ ms. The $\alpha(V)$ and $\beta(V)$ equations for dendritic CaR channels are:

$$\alpha(V) = \frac{1}{1 + e^{-(v+48.5)/3}}, \beta(V) = \frac{1}{1 + e^{(v+53)}}$$

while for the somatic CaR channels:

$$\alpha(V) = \frac{1}{1 + e^{-(v+60)/3}}, \beta(V) = \frac{1}{1 + e^{(v+62)}}$$

Finally, a calcium pump/buffering mechanism is inserted at the cell body and along the apical and basal trunk. The factor for Ca^{2+} entry was changed from $f_e = 10{,}000$ to $f_e = 10{,}000/18$ and the rate of calcium removal was made seven times faster. The kinetic equations are given by:

$$\text{drive\_channel} = \begin{cases} -f^e \times \frac{\mathrm{I_{Ca}}}{0.2 \times \mathrm{FARADAY}} & \text{if drive\_channel} > 0\ mM/ms \\ 0 & \text{otherwise} \end{cases}$$

$$\frac{d\mathrm{ca}}{dt} = \text{drive\_channel} + \frac{(10^{-4}(\mathrm{m}M) - \mathrm{ca})}{7 \times 200(\mathrm{ms})}. \tag{A16}$$

Axo-axonic, Basket, and Bistratified Cells

All compartments obey the following current balance equation:

$$C\frac{dV}{dt} = I_{\mathrm{ext}} - I_{\mathrm{L}} - I_{\mathrm{Na}} - I_{\mathrm{Kdr,fast}} - I_{\mathrm{A}} - I_{\mathrm{CaL}} - I_{\mathrm{CaN}} - I_{\mathrm{AHP}} - I_{\mathrm{C}} - I_{\mathrm{syn}} \tag{A17}$$

where C is the membrane capacitance, V is the membrane potential, I_{L} is the leak current, I_{Na} is the sodium current, $I_{\mathrm{Kdr,fast}}$ is the fast delayed rectifier K^+ current, I_{A} is the A-type K^+ current, I_{CaL} is the L-type Ca^{2+} current, I_{CaN} is the N-type Ca^{2+} current, I_{AHP} is the Ca^{2+}-dependent K^+ (SK) current, I_{C} is the Ca^{2+} and voltage-dependent K^+ (BK) current and I_{syn} is the synaptic current. The conductance and reversal potential values of all ionic currents are listed in Table 3.

The sodium current and its kinetics are described by,

$$I_{\mathrm{Na}} = g_{\mathrm{Na}} m^3 h (V - E_{\mathrm{Na}}) \tag{A18}$$

$$\frac{dm}{dt} = \alpha_m(1 - m) - \beta_m m, \quad \alpha_m = \frac{-0.3(V - 25)}{(1 - e^{(V-25)/-5})},$$
$$\beta_m = \frac{0.3(V - 53)}{(1 - e^{(V-53)/5})}$$

$$\frac{dh}{dt} = \alpha_h(1-h) - \beta_h h, \quad \alpha_h = \frac{0.23}{e^{(V-3)/20}},$$
$$\beta_h = \frac{3.33}{(1+e^{(V-55.5)/-10})}$$

The fast delayed rectifier K^+ current, $I_{Kdr,fast}$ is given by

$$I_{Kdr,fast} = g_{Kdr,fast} n_f^4 (V - E_K) \tag{A19}$$

$$\frac{dn_f}{dt} = \alpha_{n_f}(1-n_f) - \beta_{n_f} nf, \quad \alpha_{n_f} = \frac{-0.07(V-47)}{(1-e^{(V-47)/-6})},$$
$$\beta_{n_f} = 0.264e^{(v-22)/4}$$

The N-type Ca^{2+} current, I_{CaN}, is given by

$$I_{CaN} = g_{CaN} c^2 d (V - E_{Ca}) \tag{A20}$$

$$\frac{dc}{dt} = \alpha_c(1-c) - \beta_c c, \quad \alpha_c = \frac{0.19(19.88-V)}{(e^{(19.88-V)/10}-1)},$$
$$\beta_c = 0.046e^{-V/20.73}$$

$$\frac{dd}{dt} = \alpha_d(1-d) - \beta_d d, \quad \alpha_d = 1.6 \times 10^{-4} e^{-V/48.4},$$
$$\beta_d = \frac{1}{(1+e^{(39-V)/10})}$$

The Ca^{2+}-dependent K^+ (SK) current, I_{AHP} is described by

$$I_{AHP} = g_{AHP} q^2 (V - E_K) \tag{A21}$$

$$\frac{dq}{dt} = \alpha_q(1-q) - \beta_q q$$

$$\alpha_q = \frac{0.00246}{e^{(12 \times \log_{10}([Ca^{2+}])+28.48)/-4.5}}, \quad \beta_q = \frac{0.006}{e^{(12 \times \log_{10}([Ca^{2+}])+60.4)/35}}$$

$$\frac{d[Ca^{2+}]_i}{dt} = B \sum_{T,N,L} I_{Ca} - \frac{[Ca^{2+}]_i - [Ca^{2+}]_0}{\tau} \tag{A22}$$

where $B = 5.2 \times 10^{-6}/Ad$ in units of mol/(C m^3) for a shell of surface area A and thickness d(0.2 μm) and τ = 10 ms was the calcium removal rate. $[Ca^{2+}]_0$ = 5 μM was the resting calcium concentration.

The Ca^{2+} and voltage-dependent K^+ (BK) current, I_c, is

$$I_C = g_c o (v - E_K) \tag{A23}$$

where o is the activation variable. The A-type K^+ current, I_A, is described by

$$I_A = g_A ab(V - E_k) \tag{A24}$$

$$\frac{da}{dt} = \alpha_a(1-a) - \beta_a a, \quad \alpha_a = \frac{0.02(13.1-V)}{e^{(\frac{13.1-V}{10})}-1},$$
$$\beta_a = \frac{0.0175(V-40.1)}{e^{(\frac{V-40.1}{10})}-1}$$

$$\frac{db}{dt} = \alpha_b(1-b) - \beta_b b, \quad \alpha_b = 0.0016e^{(\frac{-13-V}{18})},$$
$$\beta_b = \frac{0.05}{1+e^{(\frac{10.1-V}{5})}}$$

The L-type Ca^{2+} current, I_{CaL}, is described by

$$I_{CaL} = g_{CaL} \times s_\infty^2 \times V \times \frac{1 - \frac{[Ca^{2+}]_i}{[Ca^{2+}]_0} e^{2FV/kT}}{1 - e^{2FV/kT}} \tag{A25}$$

where g_{CaL} is the maximal conductance, s_∞ is the steady-state activation variable, F is Faraday's constant, T is the temperature, k is Boltzmann's constant, $[Ca^{2+}]_0$ is the equilibrium calcium concentration and $[Ca^{2+}]_i$ is described in Eq. (27). The activation variable, s_∞, is then

$$s_\infty = \frac{\alpha_s}{\alpha_s + \beta_s}, \quad \alpha_s = \frac{15.69(-V+81.5)}{e^{(\frac{-V+81.5}{10})}-1},$$
$$\beta_s = 0.29 \times e^{-V/10.86}$$

OLM Cell

The somatic (s), axonic (a) and dendritic (d) compartments of each OLM cell obeyed the following current balance equations:

$$C\frac{dV_s}{dt} = I_{ext} - I_L - I_{Na,s} - I_{K,s} - I_A - I_h - I_{syn} \tag{A26}$$

$$C\frac{dV_d}{dt} = I_{ext} - I_L - I_{Na,d} - I_{K,d} - I_A - I_{syn} \tag{A27}$$

$$C\frac{dV_a}{dt} = I_{ext} - I_L - I_{Na,d} - I_{K,d} \tag{A28}$$

The sodium current is described by:

$$I_{Na} = g_{Na} m^3 h (V - E_{Na}) \tag{A29}$$
$$\frac{dm}{dt} = \alpha_m(1-m) - \beta_m m$$

$$\frac{dh}{dt} = \alpha_h(1-h) - \beta_h h$$

where m and h are the activation and inactivation variables, respectively. The conductance and reversal potential values per compartment are listed in Table 4. The forward and backward rate constants are described by:

$$\alpha_{m,\text{soma/axon}} = \frac{-0.1(V+38)}{\exp(\frac{-(V+38)}{10})-1}, \qquad \beta_{m,\text{soma/axon}} = 4\exp\left(\frac{-(V+63)}{18}\right)$$
$$\alpha_{h,\text{soma/axon}} = 0.07\exp(\frac{-(V+63)}{20}), \quad \beta_{h,\text{soma/axon}} = \frac{1}{1+\exp(\frac{-(V+33)}{10})}$$
$$\alpha_{m,\text{dend}} = \frac{-0.1(V+45)}{\exp(\frac{-(V+45)}{10})-1}, \qquad \beta_{m,\text{dend}} = 4\exp(\frac{-(V+70)}{18})$$
$$\alpha_{h,\text{dend}} = 0.07\exp(\frac{-(V+70}{20}), \qquad \beta_{h,\text{dend}} = \frac{1}{1+\exp(\frac{-(V+40)}{10})}$$

The potassium current, I_K, is described by:

$$I_K = g_K n^4 (V - E_K) \tag{A30}$$

$$\frac{dn}{dt} = \alpha_n(1-n) - \beta_n n$$

where n is the activation variable for this channel. The conductance and reversal potential values per compartment are listed in Table 4. The forward and backward constants are described by:

$$\alpha_{n,\text{soma/axon}} = \frac{-0.018(V-25)}{\exp(\frac{-(V-25)}{25})-1}, \quad \beta_{n,\text{soma/axon}} = \frac{0.0036(V-35)}{\exp(\frac{V-35}{12})-1}$$

$$\alpha_{n,\text{dend}} = \frac{-0.018(V-20)}{\exp(\frac{-(V-20)}{21})-1}, \quad \beta_{n,\text{soma/axon}} = \frac{0.0036(V-30)}{\exp(\frac{V-30}{12})-1}$$

The transient potassium current, I_A, is described by:

$$I_A = g_A a b (V - E_k) \tag{A31}$$

$$\frac{da}{dt} = \frac{(a_\infty - a)}{\tau_a}, \quad a_\infty = \frac{1}{(1+\exp(\frac{-(V+14)}{16.6}))}, \quad \tau_a = 5ms$$

$$\frac{db}{dt} = \frac{(b_\infty - b)}{\tau_b}, \quad b_\infty = \frac{1}{(1+\exp(\frac{-(V+71)}{7.3}))}, \quad \tau_b = \frac{1}{\alpha_b + \beta_b}$$

where a and b are the activation and inactivation variables, respectively. The rate constants are given by:

$$\alpha_b = \frac{0.000009}{\exp(\frac{V-26}{18.5})} \quad , \quad \beta_b = \frac{0.014}{0.2+\exp(\frac{-(V+70)}{11})}$$

The nonspecific cation channel, I_h, is described by:

$$I_h = g_h r (V - E_r) \tag{A32}$$

$$\frac{dr}{dt} = \frac{(r_\infty - r)}{\tau_r}$$

where r is the activation variable for this channel. The conductance and reversal potential values per compartment are listed in Table 4. The steady state activation curve and time constant are given by:

$$r_\infty = \frac{1}{(1+\exp(\frac{V+84}{10.2}))},$$
$$\tau_r = \frac{1}{\exp(-17.9-0.116V)+\exp(-1.84+0.09V)} + 100$$

Septal Cells

Septal cell output was modeled as bursts of action potentials using a presynaptic spike generator. A spike train consisted of bursts of action potentials at a mean frequency of 50 Hz for a half-θ cycle (125 ms; corresponding to a recall period) followed by a half-θ cycle of silence. Due to 40% noise in the interspike intervals, the 10 spike trains in the septal population were asynchronous.

Entorhinal Cortical Cells

EC cells were also modeled as noisy spike trains, using a presynaptic spike generator. A spike train consisted of spikes at an average gamma frequency of 40 Hz, but with individual spike times Gaussian-distributed around the regular ISI of 25 ms, with a standard deviation of 0.2. The population of EC inputs fired asynchronously.

CA3 Pyramidal Cells

CA3 pyramidal cells were modeled as spike trains of the same form and with the same characteristics (mean frequency and noise level) as the EC cells. Onset of CA3 firing was delayed by 9 ms relative to the EC trains to model the respective conduction delays of direct and trisynaptic loop inputs to CA1.

Synaptic Currents

All synaptic currents were modeled using dual exponential conductance waveforms. The parameters for the synaptic currents used are listed in Table 5. All connection strengths (maximum conductances) of the different pathways are listed in Table 6.

Pyramidal cell

Axonic (a) and somatic (s) compartments receive GABA-A inhibition from axo-axonic and basket cells, respectively. The radiatum-proximal (RadProx) compartment receives recurrent excitation via AMPA synapses from its neighboring P cells, whereas the radiatum-medium (RadMed) compartment receives both AMPA and NMDA excitation from the CA3 Schaffer collateral input and GABA-A and GABA-B inhibition from the bistratified cells. The RadMed AMPA synapse is plastic and changes according to the Eqs. (1)–(4). The lacunosum-moleculare thick (LM-T) com-

partment receives AMPA excitation from the EC perforant path and GABA-A and GABA-B inhibition from the OLM cells.

Axo-axonic cell

Radiatum-thick (Rad-T) and radiatum-medium (Rad-M) compartments received AMPA excitation from the CA3 Schaffer collateral input. LM-medium (LM-M) compartment received AMPA excitation from the EC perforant path input, whereas the Ori-T compartment received AMPA excitation from the P cell feedback excitation and GABA-mediated inhibition from the septum.

Basket cell

Radiatum-thick (Rad-T) and radiatum-medium (Rad-M) compartments received AMPA excitation from the CA3 Schaffer collateral input. LM-medium (LM-M) compartment received AMPA excitation from the EC perforant path input, whereas the Ori-T compartment received AMPA mediated excitation from the P cell feedback excitation and GABA-mediated inhibition from the septum. The somatic compartment received GABA-A synaptic inhibition from neighboring basket and bistratified cells.

Bistratified cell

The radiatum-thick (Rad-T) and radiatum-medium (Rad-M) compartments received AMPA synaptic excitation from the CA3 Schaffer collateral input. The somatic compartment received GABA-A inhibition from neighboring bistratified cells. The Ori-T compartment received AMPA excitation from the P cell feedback excitation and GABA-mediated synaptic inhibition from the septum.

OLM cell

Each OLM cell received AMPA excitation in their dendrites from the P cells and GABA-mediated inhibition from the septum.